UNIVERSITY OF CALIFORNIA SAN DIEGO

Miniature Microscopy for Biological Applications

A dissertation submitted in partial satisfaction of the
requirements for the degree
Doctor of Philosophy

in

Electrical Engineering (Photonics)

by

Pavel Shekhtmeyster

Committee in charge:

Professor Sadik Esener, Chair
Professor Axel Nimmerjahn, Co-Chair
Professor Joseph Ford
Professor Yu-Hwa Lo
Professor Donald Sirbuly

2019

The dissertation of Pavel Shekhtmeyster is approved, and it is acceptable in quality and form for publication on microfilm and electronically:

_____

_____

_____

_____
Co-Chair

_____
Chair

University of California San Diego

2019

DEDICATION

Dedicated to my love, Moae.

You are the lens which brings my world into focus.

TABLE OF CONTENTS

LIST OF FIGURES

LIST OF TABLES

ACKNOWLEDGEMENTS

I would like to acknowledge Professor Nimmerjahn as my PI and Co-Chair. Thank you for taking me into your lab at the Salk Institute, teaching me about neuroscience, and for being patient with my ever-evolving schedule and slightly helter-skelter working and communication style...

I would also like to acknowledge my Chair, Prof. Esener, for accepting me into his group and always lending a helping hand.

I would like to thank my enduring Committee member, Prof. Lo, and the two, gracious last-minute additions, Prof. Ford and Prof. Sirbuly, as well as my former Committee members who could not make it: Prof. Heller and Prof. Wang.

I would also like to acknowledge my colleagues in the lab whose efforts directly led to my success (listed in an order randomly generated via Matlab algorithm): Our ever-patient with my lateness, Daniela (Cook) Duarte (I'll definitely make it on time to our next scheduled experiment...). Our mouse-diaper changer, Robert Folk. Our head of IT, Alex Ngo. Our generous delicious tea and food sharer, Xiang Wang. Our resident rock star and former actor, Chuck Clark (who never treated us like mushrooms).Our ever-helpful Erin Carey, thanks for putting up with my loud and intense nonsense. Our resident and ex-resident Zumba experts, Katharina Merten and Yusuf Tufail, thanks for teaching me cool things about biology and about the finer points of grad school life. Our ex-lab children, you grew up so fast... Our ex-resident world traveler and sweet potato expert, Kohei Sekiguchi.And our junior grad student, Nicholas Nelson (congratulations on your promotion to senior grad student! You're in charge now, good luck!

I would like to acknowledge the efforts of all the grad students out there who also have ADHD...it is possible! (P.S. go to therapy, it helps)

And, to my family, and especially to my mom. Thank you for always being supportive and kind, and for always believing in me.

Finally I would like to acknowledge the efforts of Moae, who stayed awake through

countless nights with me, reading and rereading, editing and reediting. You helped me focus my chaos of facts into a point of truth. Without you this dissertation could not happen.

Chapter 3 contains text from a publication as it appears in Imaging large-scale cellular activity in spinal cord of freely behaving mice, 2016. Sekiguchi, K. J., Shekhtmeyster, P., Merten, K., Arena, A., Cook, D., Hoffman, E., Ngo, A. & Nimmerjahn, A. Nat. Commun. 7, 11450 (2016). The dissertation author was an investigator and second author of this paper.

Chapter 4, in part, is currently being prepared for submission for publication of the material. Shekhtmeyster, Pavel; Nimmerjahn, Axel. The dissertation author was the primary investigator and author of this material.

VITA

2008	B.S. in Electrical Engineering, University of California San Diego
2013	M.S. in Electrical Engineering (Photonics), University of California San Diego
2019	Ph.D. in Electrical Engineering (Photonics), University of California San Diego

PUBLICATIONS

Sekiguchi, K. J., Shekhtmeyster, P., Merten, K., Arena, A., Cook, D., Hoffman, E., Ngo, A. & Nimmerjahn, A., "Imaging large-scale cellular activity in spinal cord of freely behaving mice", Nat. Commun. 7, 11450, (2016).

ABSTRACT OF THE DISSERTATION

Miniature Microscopy for Biological Applications

by

Pavel Shekhtmeyster

Doctor of Philosophy in Electrical Engineering (Photonics)

University of California San Diego, 2019

Professor Sadik Esener, Chair
Professor Axel Nimmerjahn, Co-Chair

Miniature epifluorescent microscopy has enabled functional imaging of the central nervous system in awake, freely-moving animals; this dissertation describes work on three such devices. Using the Salk Miniscope, our lab was first to demonstrate spinal cord imaging in freely-behaving mice. Gargantua, a color-corrected miniature microscope, has demonstrated three-color imaging with improved resolution, contrast, and working distance. Odin, a design for a mouse-borne miniature mesoscope, is expected to image a 3.84mm x 2.88mm field of view with a 0.6μm PSF.

Chapter 1

Introduction

In recent years, there has been increased interest in imaging in vivo, awake, freely-behaving animals, especially since certain types of cellular activity are potentially suppressed by anesthesia [1]. As result, in vivo miniature microscopes have seen marked improvements in their imaging quality and portability, with multiple devices described in the literature [2], [3], [4], [5], [6], [7], [1]. Designs have focused on improving microscopes' capabilities of more accurately resolving smaller objects, and resolving across a larger field of view. These capabilities have allowed for a more accurate understanding of cellular and sub-cellular dynamics, as well as the interaction of entire cellular networks.

Therefore, I set out to design miniature microscopes that performed well for a broad range of biological applications, were modular to aid the implementation of any improvements, and highly adaptive to allow multiple configurations during one session of exploratory work. The first device presented in this work, called the 'Salk Miniscope', was inspired by a previously published microscope [2] with improvements made to the field of view, resolution, and sensitivity. This effort led to the work published in Sekiguchi, et al. 2016 [1]. Learning from the design and fabrication process, I designed a second miniature microscope, named 'Gargantua' for its small stature. This color-corrected miniature microscope made improvements on the Salk Miniscope in

the areas of color-imaging capability, working distance, and imaging quality. The third and final device was created to meet the needs of our lab to observe cellular activity across a larger field of view. I named this miniature mesoscope 'Odin', in reference to the large FOV, as Odin, from Norse mythology, is referred to as the 'All-Seeing-One'. This miniature mesoscope would give our lab a competitive edge, as currently, in the field of mesoscopes, we are only aware of one other miniature version that has been published, and it is limited to imaging larger animals (rats) [7].

1.1 Dissertation Organization

The dissertation is organized into several chapters. Chapter 2 describes my methods used for characterizing the microscopes. Chapter 3, 4, and 6 are dedicated to each miniature microscope. Each of these chapters includes an explanation of the design of the device, the characterization data of the integrated device, and any explanations of deviations from the methods described in Chapter 2. I also discuss any notable differences between design expectations and integrated device performance, improvements for future designs, and current and future applications of the device. Chapter 5 is dedicated to my contribution to the software pipeline used for analyzing data collected with Gargantua, parts of which are also applicable to data collected by the Salk Miniscope and Odin.

Chapter 2

Methods for Characterization

During the research phase, I found that there was a distinct lack in the standardization of how miniature microscope characterization data was presented. Data would often be presented in different formats using different metrics. For example, the 'cellular resolution' would often be presented, but the results held a vastly variable meaning as the value depended on what types of cells were being observed, as well as the labeling density (the number of fluorescent cells per unit area both laterally and axially). Additionally, distinctions were not made between optical system performance and image-quality improvements obtained through software-based post-processing (e.g. spatial down-sampling, PCA/ICA, etc.). Therefore, I present my integrated device characterization within the categories that I believe are most applicable to real-world imaging, so I may more accurately characterize their functionality and performance, as well as make comparisons across several devices easier and more intuitive. This framework is broken up into four categories: Physical Attributes, Optical Parameters, Digital Quantization, and Imaging. What follows are the methods I used to calculate or measure the characterization data. Unless noted in the specific microscope chapter, these methods were used to characterize all three microscopes.

2.1 Physical Attributes

The first category, 'Physical Attributes', includes the size and weight of the microscope. This is a key category as size and weight determine what kinds of animals can be used for experiments. Our lab primarily focuses on studying murines for neuroscience research. Mice are often preferred over rats as they have more well-developed transgenic lines and tools for research. A mouse can carry ~20% of its weight, and if the average mouse is ~20g, a device designed to image freely-moving, naturally-behaving mice should be less than 4g. Size was defined as the length x width x height in millimeters of the integrated device. The weight was defined as the total weight of the optics, filters, integrated illumination module, housing, image sensor, and sensor PCB, but not the sensor cabling wires or optical fibers as the weight of these would be supported by external mounts or a commutator. The weight was measured by weighing the integrated system using a laboratory scale.

2.2 Optical Parameters

The second category, 'Optical Parameters', includes numerical aperture (NA), working distance, and field of view (FOV).

NA is an important parameter as it specifies the light-collection ability of the microscope, which impacts imaging-quality and reduces the potential for photo-toxicity induced in the animal. As NA was a parameter that was difficult to measure in this miniaturized format, I presented the NA value as was determined by the design.

Working distance is an important parameter as it determines the mounting distance of the microscope, and the ability to utilize intermediary optics. A longer working distance is preferred as it allows for a larger acceptable margin of error for surgical preparations of the imaging window. Imaging with intermediary optics allows for novel applications, one being prism-assisted imaging.

Prism-assisted imaging allows for deep imaging along the axial dimension, which is desirable for certain types of neurological research [8]. Though the exact working distance does depend on the position of the image sensor along its focusing track, as well as the thickness of the cover glass (for our in vivo experiments we used a #0 cover glass which is ~100μm thick), for the purposes of standardization, I defined working distance as the edge of the objective barrel to the target in air. I measured the working distance of the integrated device using a precision differential actuator (micrometer) with a 0.5μm resolution (DRV3, Thorlabs) and an imaging target with a 100μm-spaced grid, printed on the surface of a glass substrate, sans cover glass. I positioned the image sensor approximately in the middle of its focusing track, clamped the integrated device to a three-axis translation stage, and measured the axial displacement to where the image was in focus (I counted the axial rotations of the micrometer until the image was in focus).

The field of view is an important parameter as it determines the extent of cellular networks and the size of the cellular populations that can be observed. FOV is determined by design and is dependent on nominal magnification and the size of the sensor. I measured the FOV of the integrated devices using the micrometer (DRV3, Thorlabs) and the 100μm grid target. I positioned the image sensor approximately in the middle of its focusing track, clamped the integrated device to a three-axis translation stage, and brought the image to focus. Next, I aligned the left edge of the image to a grid line and counted the number of entire visible grid squares in one row. To calculate the remaining distance that was less than one grid square (100μm), I translated the image along the x-axis, measuring the lateral displacement until the right-edge of the image aligned to the next grid line. This was repeated for the y-axis.

2.3 Digital Quantization

The third category is 'Digital Quantization', as defined across time, space, and intensity, and is determined by the electronics of the image sensor. This includes characteristics of the

sensor such as frame rate, pixel spacing, and sensor bitdepth/intensity quantization.

The frame rate is important because it determines the temporal resolution with which one can sample cellular dynamics, as well as determines the ability to correct lateral motion artifacts. Pixel resolution is the total number of pixels in the image sensor, and pixel spacing is the size of one pixel at the object plane. Pixel spacing is an important category to report because it determines the spatial sampling of the optical image, as defined by the Shannon-Nyquist Theorem. For highest-quality imaging, pixel spacing should be equal to one-half of the optical point spread function (PSF). Sensor bitdepth/intensity quantization is the digital intensity resolution and defines the number of intensity levels (or steps) that the image sensor records. The sensor bit depth is important because it determines how small of a change in fluorescence intensity the device can distinguish. All of these sensor characteristics were obtained from the sensor's data sheet.

2.4 Imaging

The final category is 'Imaging', which includes imaging quality (both resolution and contrast) and color-imaging capability. All measurements were taken prior to any image processing enhancements to characterize the optical performance of the integrated device.

The term 'resolution' is potentially ambiguous as it could be used to refer to either the image sensor resolution or the optical resolution. The image sensor resolution is only a partial representation of imaging quality as it does not correspond to optical resolution. This is because the number of pixels in an image does not correlate to sharpness – the optical system determines the sharpness, and increasing the number of pixels will not improve the imaging quality for an optical system that cannot resolve the desired object size (i.e. it is equivalent to over-sampling the image without increasing the information content). Therefore, it is important to provide both sensor and optical specifications for a full characterization of integrated devices. For fluorescence

microscopy, which relies on non-coherent imaging (recorded information is linear in terms of intensity), I believe the linear system formalism of the PSF can be used to describe the resolution as it is the impulse-response of the focused imaging system.

I characterized the optical resolution both at the center and across the FOV because high resolution at the center does not guarantee the same performance across the FOV. To measure the resolution I used the point spread function (PSF) and the limit of resolution (LOR) test. I measured PSF at the center of the FOV, and used the LOR test to approximate the PSF across, and at the edges of, the FOV, because while the PSF is fairly simple to measure once (in the center of the FOV), it becomes increasingly time-consuming to measure across the FOV.

Measurement of Resolution via the Point Spread Function

To measure the PSF in the center I generated a point source using a 0.5μm pinhole (TC-RT01, Technologie Manufaktur), green fluorescence reference slide (2273, Ted Pella), and blue LED excitation source (M470L3, Thorlabs). First, I defocused the image until no contrast could be observed by eye. Then, I recorded multiple images in evenly-spaced axial intervals while focusing/translating the microscope going through focus (to a focused point and through to no contrast). I then used software (ImageJ or MATLAB) to calculate the lateral and axial maximum intensity projections, then measured the cross-section data by taking a line profile across the center of each Airy disc; for the axial PSF cross section I took the cross section along the z-axis. I defined the width of the PSF as full width at half maximum (FWHM) of a one-dimensional Gaussian function fitted to the cross-section profile of the measured lateral and axial PSFs. The fitting of the Gaussian profile was accomplished in ImageJ using a custom script or MetroloJ software [9, **?**] or in MATLAB using a script created by Katharina Merten. All analyses were performed on raw, unprocessed data.

Measurement of Resolution via the Limit of Resolution Test

For the LOR test I used a High-Resolution Microscopy Target (TC-RT01, Technologie Manufaktur), a modified version of a bar-set test chart, with the maximum spatial frequency extended up to 3300lp/mm. Though the classic LOR test uses the 1951 USAF Resolution Test Chart, it is limited in its applicability to microscope testing due to the limit in the highest spatial frequency (645.1 lp/mm for stock #55-622, Edmund Optics). The LOR test was performed at five points along the x-axis: the center of the FOV, 25% away from the center, and at the edges (at 46% away from the center). The focus was aligned to the center point and kept stable across the radial positions to account for field curvature and astigmatism. Traditionally, the LOR test asks multiple observers to identify the smallest set of bars which are resolvable (visually distinguishable) to them - the next smaller set, which is not resolvable (visually indistinguishable), is labeled as the limit of resolution. As these results would be highly subjective to eyesight and individual interpretation of 'resolvable', I instead used software to calculate the LOR. First, I plotted the line profile across the bar variance and averaged along the bar length, averaged the peaks and troughs, and calculated the contrast percentage using the Michelson contrast equation

$$\frac{I_{max} - I_{min}}{I_{max} + I_{min}}$$

I performed these calculations with the aid of a custom script and the 'Find Peaks' ImageJ plugin [10, **?**].Since the average human eye can discriminate hard-edge shapes with 1.2-3.0% contrast in low spatial frequencies [11, 12, 13], and 5% in high spatial frequencies [14, 15], I defined the LOR limit (highest spatial frequency) by the bar set where at least 5% contrast could be observed.

Measurement of Contrast via the Modulation Transfer Function

In addition to resolution, it is important to define the contrast capabilities of the microscope as the imaging quality, and subsequently the ability to retrieve information, can be limited by

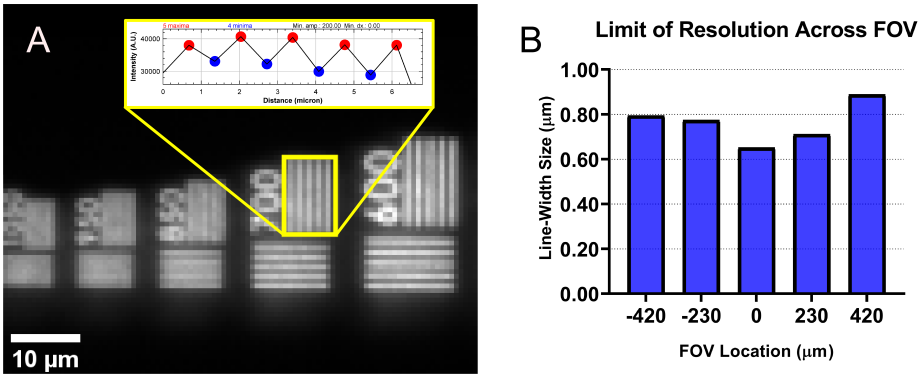

Figure 2.1: Gargantua microscope: A) An example of a test chart image displaying the resolution limit. B) The LOR measurements across the FOV in line-widths (μm).

contrast, independent of resolution. Contrast is the brightness of the object relative to background calculated via the Michelson contrast equation. This capability is especially important to define for fluorescence imaging experiments involving the observation of tissue with dense-labeling in the presence of a fluorescent background. Since optical systems typically decrease the contrast of the imaged object, I believe the modulation transfer function (MTF) is the most appropriate way to determine contrast as it defines the contrast of the optical image relative to the contrast of the actual object. Though MTF could theoretically be calculated from PSF, I do not do so as the PSF is difficult to measure with high enough precision. As MTF values are unique to each imaging system, an MTF plot demonstrates the contrast relative to object-size in terms of spatial frequency. It is not appropriate to compare square-wave based MTF measurements against the standard sinusoidal-based MTF, so comparisons of Slanted Edge MTF to MTF measurements that are calculated using bar charts (i.e. 1951 USAF Chart, star charts, etc.) should be avoided as those measurements will be 10-15% higher than the associated standard sinusoidal MTF [16]. Like resolution, I measured MTF both at the center and across the FOV since good performance at the center does not guarantee the same performance across the FOV. To measure the MTF I used the Slanted Edge test, as based on my experiences, it was both simple to measure and reliable to replicate. I calculated the sagittal and tangential MTF in the center and in two radial

positions from the center (again at 25% and at 46%), at the same positions as the LOR tests. The slanted edge target was generated using a razor blade, and I used the same green fluorescence reference slide and blue LED excitation source used to measure PSF (2273, Ted Pella; M470L3, Thorlabs). The optimal focus position was found for the center of the FOV, and then kept the same for images away from the center. Analysis was performed using the 'Slanted Edge MTF' ImageJ plugin [17] and a custom MATLAB script I made (see Appendix) was used for plotting.

Alignment of images and analysis was performed as follows: each location was converted to pixel coordinates and the sensor control software was used to mark the location on the screen. The target was then translated until the slanted edge matched the marked location. During analysis, a custom ImageJ macro (see Appendix) was used to generate an ROI in the image, centered on the location under test; the ROI was used for the slanted edge quantification. An ROI of the same size was used for all locations under test. The images of the slanted edge were then analyzed using the Slanted Edge MTF ImageJ plugin and a custom MATLAB script. The MTF is calculated from the Edge Spread Function, taken across the region of transition between the black and white regions; the calculation uses 64 lines to perform the calculation. I used a custom ImageJ macro to draw a rectangular ROI centered on the same pixel as the one I aligned the slanted edge to during recording. The macro also allowed me to draw ROIs of the same width and height across all the imaging locations every time.

Since the quality of the imaging sample and its preparation play a significant role in imaging quality, I presented the spatial frequency of the MTF at 10%, 20%, and 50%, as they represent labeling of increasing densities and therefore are relevant across a large range of applications. Although values of MTF at 0% are frequently reported, I do not believe they are reliable as values below 10% tend to be affected by sensor noise limits and optical phase reversal.

Lastly, in order to make comparisons across devices for use in biological applications easier and more intuitive, I presented the conversions of the MTF and LOR spatial frequency values to line-widths. A line-width is equal to one-half the spatial period. These values were

calculated by averaging the sagittal and tangential components, as they are orthogonal, and in an incoherent imaging system such as fluorescent recordings, the average represents a good approximation of true optical performance.

Measurement of the Color-Imaging Capability

Color-imaging capability is included in the category 'Imaging' as it is a key function in miniature microscopes that allows for the observation of multiple genetically-distinct types or sub-types of cells. Most miniature microscopes are designed to image only one spectral band (the emission of a single fluorescent reporter). Successful multi-color imaging occurs when objects emitting multiple spectral bands are recorded with all objects in focus, with sufficiently low axial chromatic aberration. To confirm and demonstrate the capability of multi-color imaging, I imaged 15μm fluorescent polystyrene beads of three spectral bands: yellow-green (505nm/515nm), yellow (515nm/534nm), and red (580nm/605nm) (F8844, F21011, F8842, ThermoFisher). This test also was used to confirm the capability of my post-processing pipeline to separate three spectral bands efficiently. This method was only used to characterize Gargantua as it was the only multi-color microscope tested.

2.5 Measurement Vignetting

When discussing the performance of an integrated imaging device, it is important to consider vignetting. Vignetting describes the variation of light gathering ability across different positions of the FOV. Typically, vignetting manifests as a darkening of the image toward the edges, and results in reduced signal-to-noise ratio in the image periphery. Vignetting can result from the constriction of a field aperture within the imaging pathway of the microscope. The illumination pathway of an epifluorescent microscope can also contribute to vignetting via an asymmetry in the illumination field. Vignetting can be quantified by imaging a homogeneously

fluorescent sample. Using an external illumination sources allows for isolating the vignetting contribution of the imaging pathway. Using a microscope's integrated illumination sources allows for quantifying the vignetting of the integrated device.

To measure vignetting, I focused on the surface, and recorded an image, of a fluorescent test slide (2273, Ted Pella). Where necessary, I used a blue LED source (M470L3, Thorlabs) as the source of external illumination.

Chapter 3

‘Salk Miniscope’

Miniature One-Photon Microscope

In Ghosh et al. 2011, a one-photon, monochromatic, epifluorescent, miniature microscope was described [2] (referred to here as the “Stanford Miniscope”). Our goal was to build a similarly performing microscope following the published work and to modify it to meet our specific research needs. Very little was known about how sensory information from mechanoreceptors and nociceptors in the skin is encoded by spinal cord cell types and their activity patterns, particularly under freely behaving conditions. These receptors play key roles in adaptive and protective motor behavior (touch and pain encoding in the spinal cord).

Therefore, we sought out to develop a miniature, one-photon microscope that would allow stable measurement of neuronal and glial cell activity in behaving mice, which would complement the two-photon approach already in use in the lab. Several improvements were made when compared to the Ghosh et al. design, the most notable being the use of an updated image sensor, leading to improved field of view, resolution, and sensitivity.

Additionally, during bench-testing, several performance issues not addressed in the Ghosh et al. publication motivated the redesign of several components, as described in ‘Design

Improvements' below. Ultimately, this effort led to the work published in Sekiguchi, et al. 2016 in which we described the cellular and computational logic of spinal cord networks under certain behaving conditions [1].

3.1 System Design

In the sections that follow, I describe the components that performed similarly to the Ghosh et al. work (filters, imaging path optics, housing, and illumination), the components that were improved upon from the original design (image sensor and illumination driver), and redesigns implemented to address problems discovered during bench-testing.

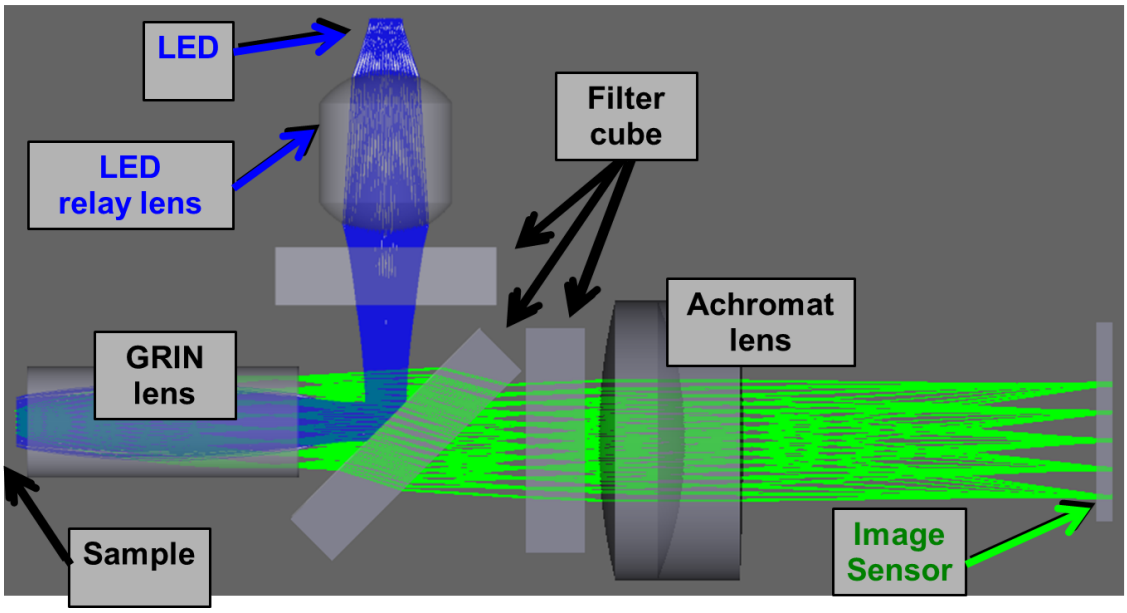

Figure 3.1: Optical layout of the Salk Miniscope device. The imaging path is along the horizontal direction, with the animal on the left, and the image sensor on the right. During in-vivo imaging, the microscope was mounted above the animal, with the orientation rotated 90°counterclockwise relative to the above image.

3.1.1 Design Similarities

The Stanford Miniscope used commercially available lenses, a custom housing, and commercial fluorescent filters custom-sized to fit the housing; we adopted a similar approach.

Optics: Imaging Path

The Salk Miniscope imaging path utilized two lenses: a gradient index (GRIN) lens as the objective (GT-IRFL-200confD-50, GRINTech GmbH, 0.23mm pitch), and an achromatic doublet as the tube lens (#45-207, Edmund Optics). I used Zemax software package (Zemax LLC) to design the optical system of the Salk Miniscope, to match the performance described in the Ghosh et al. work. Figure 3.3 shows the optical prescription of the Salk Miniscope.

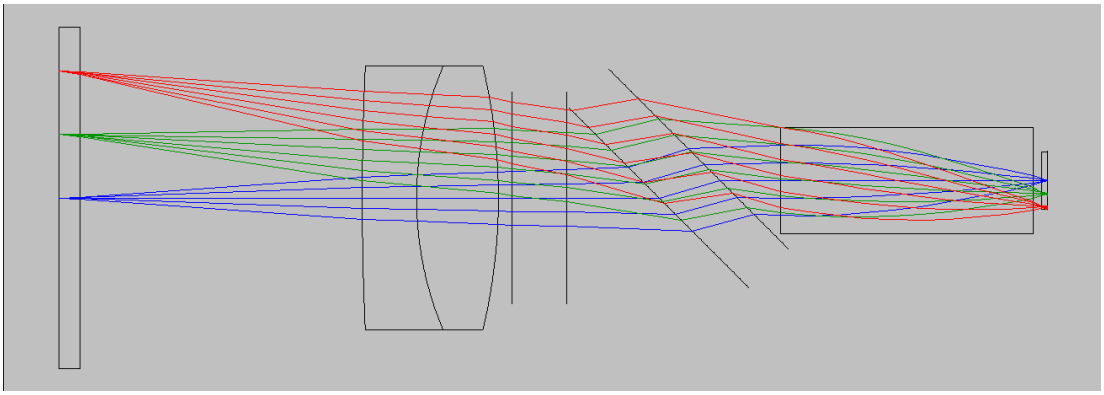

Figure 3.2: Imaging pathway of the Salk Miniscope.

Housing

Using the publication and the requirements of my Zemax model, our software engineer at the time, Christopher Aprea, developed the housing using the 3D modeling software SketchUp (Trimble Inc).

Surf	Type	Radius	Thickness	Glass	Diameter
OBJ	STANDARD	Infinity	0.4	N-BK7	4.8
1	STANDARD	Infinity	5.35		6.46
2	STANDARD	53.57	1.03	N-SF10	5
3	STANDARD	6.46	1.55	N-BAF10	5
4	STANDARD	-10.67	0.25		5
5	STANDARD	Infinity	1.05	F_SILICA	4
6	STANDARD	Infinity	1.746		4
7	COORDBRK	-	0		-
8	STANDARD	Infinity	1.05	F_SILICA	4.8
9	STANDARD	Infinity	-1.05		4.8
10	COORDBRK	-	1.05		-
11	STANDARD	Infinity	1.25		3.175449
12	COORDBRK	-	0		-
STO	GRINSUR5	Infinity	4.786293	GTAG	2
14	STANDARD	Infinity	-4.786293		2
15	COORDBRK	-	4.786293		-
16	STANDARD	Infinity	0.2704651		1.232194
17	STANDARD	Infinity	-0.1		1.133711
18	STANDARD	Infinity	0.1	N-BK7	1.083404
IMA	STANDARD	Infinity			1.086363

Figure 3.3: Optical prescription of Salk Miniscope.

Illumination

The illumination path was constructed from a drum lens (#45-549, Edmund Optics), and a miniature LED (LXML-PB01-0030, LUXEON Rebel, Phillips) mounted on a custom 0.275 x 0.330 x 0.037inch heatsink.

Filters

Fluorescence filters were chosen to match the excitation and emission spectra of the functional calcium indicators available at the time: the chemical-dye Oregon Green BAPTA (OGB) and the genetically-encoded calcium protein (GCaMP3). We used the following fluorescence filters, all from Chroma Technology Corp: excitation, emission, and dichroic beam-splitter filters: ET480/40x (4 x 4 x 1.1mm) for excitation, ET535/50m (4 x 4 x 1.0mm) for emission, and T495LPXR (4 x 4.8 x 1.0mm) for the dichroic beam-splitter. Early tests were conducted using ET480/40x, ET525/36m, and T500LPXT, also from Chroma Technology Corp.

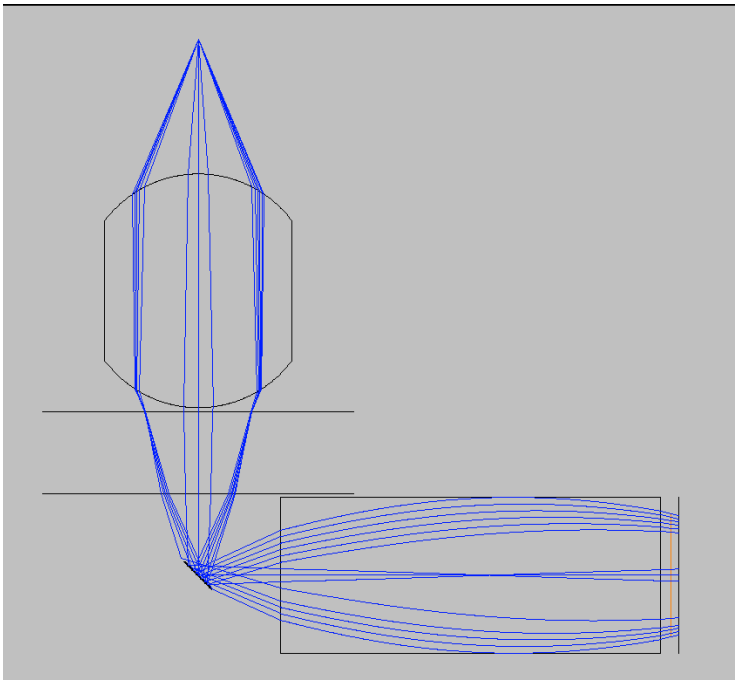

Figure 3.4: Illumination pathway of the Salk Miniscope.

3.1.2 Design Improvements

In a effort to obtain performance results more aligned with our research goals, we utilized a different image sensor and the illumination driver.

Image Sensor

We selected the MT9M024 CMOS sensor (Aptina Imaging Corp.) based on improvements to the field of view, sensitivity, and pixel resolution, as outlined below in Table 3.1. The quantum efficiency of the sensor is show in Figure 3.5. The sensor had a rolling shutter and was capable of imaging at 45.45 frames per second (fps) using the full pixel resolution of 1280x960. The sensor was capable of faster image acquisition at a reduced pixel resolution. The image sensor active area measured 4.8 x 3.6mm.

In order to operate the image sensor, we designed and fabricated a miniature sensor board to mount the sensor, selected a receiver board to facilitate communication from the sensor to the

Table 3.1: Comparison of sensor performance between the Stanford Miniscope and Salk Miniscope, showing significant improvement in multiple categories.

	Stanford Miniscope Image Sensor	Salk Miniscope Image Sensor	Improvement
Pixel Size	5.6μm	3.75μm	$\sim$50%
Sensor Active Area	3.6 x 2.7mm	4.8 x 3.6mm	$\sim$78%
Sensitivity	1.9V/lux-sec	6.7V/lux-sec	$\sim$252%
Frame Rate	30fps	45fps	$\sim$50%

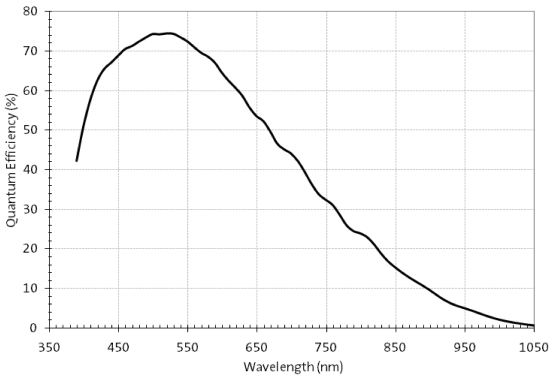

Figure 3.5: Estimated quantum efficiency of MT9M024 image sensor. Reproduced from Aptina MT9M024 datasheet.

computer, and fabricated custom cabling to connect the two.

I chose the ball-grid array (BGA) package as it was the smallest package, in size and weight, available for this sensor model. The image sensor package had 63 connector leads, but in order to minimize the weight of the device and to maintain the flexibility of the cabling, I created a model to determine the bare minimum of functional components required for sensor operation (such as power sources, which power sources could be combined, clock generation, communication lanes, etc.). In the end, I determined that only 10 wires needed to be used for: power, ground, positive and negative I2C sensor control protocol, two wires for clock signal,

and four wires for HiSPi data transmission protocol (2-Lane SP-packetized).This information was given to an engineering firm, AxelSys, which designed the circuit model with off-the-shelf components as well as the printed circuit board (PCB) layout.

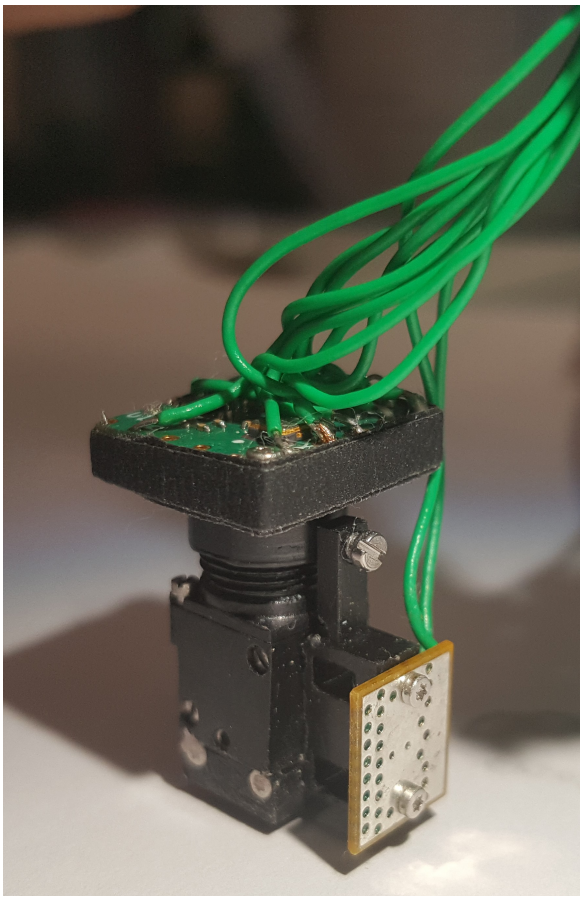

Figure 3.6: Image showing Salk Miniscope with 10 sensor wires.

In order to facilitate communication between the sensor and the computer, the Demo2x receiver board and the HiSpi adapter board were used (MT9S6NNB03, Aptina Imaging Corp. and APT-C4AV-S6NNR04, Center for Artificial Vision, respectively). Communication between the receiver board and the computer was performed using the Aptina DevWare Software Package. Data transmission between the sensor and the receiver board was performed using the Aptina HiSPi transmission protocol. As per Aptina technical literature and my communications with

Aptina engineers, this protocol was originally designed for high-bandwidth transmission through a ribbon cable with a maximum length of 15cm. After performing calculations and bench-testing, I was able to extend the range of the HiSPi protocol to 200cm by transmitting in "High VCM" regime over twisted-pair connections.

Illumination Driver

The Ghosh, et al. 2011 publication described an issue with heating of the diode junction of the integrated LED, which caused a downward drift in the illumination intensity on a scale comparable to the functional fluorescent signals under observation. The drift in the intensity of the Stanford Miniscope appeared in the beginning of each recording, and stabilized after approximately one minute, as the temperature of the LED reached equilibrium; however, as typical experimental recordings lasted $\sim$5 minutes, this intensity drift was a significant issue. Ghosh et al. used a pulse-width voltage-modulation driver to control the LED intensity. To address the issue of intensity drift, Ghosh et al. characterized the drift for each individual LED unit, then developed a digital controller for the LED driver which increased the LED intensity in steps to counteract the drift, based on the characterized profile of each LED.

I proposed an alternative solution for the Salk Miniscope, using an analog current-feedback driver. The driver was fabricated by our in-house electronics shop (Thuy Nguyen, Salk Institute). This solution allowed for stabilized control of the LED intensity by utilizing current feedback to monitor and correct the illumination intensity drift. Figure 3.7 compares the performance of a pulse-width voltage-modulation LED driver, similar to one used by Ghosh et al., with the current-feedback LED driver. The current-feedback driver reduced intensity drift and transient fluctuations, eliminating the need to calibrate and test individual LEDs.

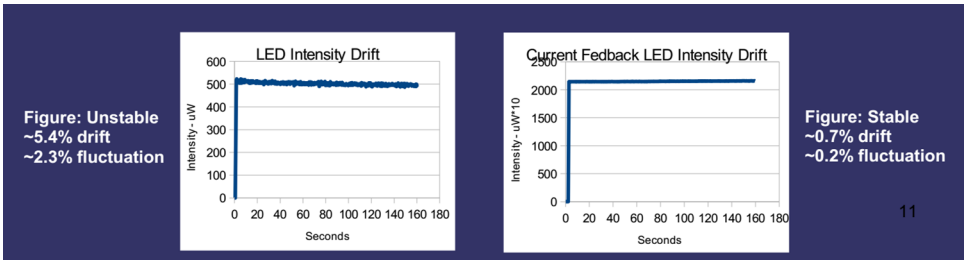

Figure 3.7: Improvements to illumination stability by utilizing current feedback driver. Left – integrated LED intensity drift when using a constant-voltage driver with pulse width modulation. Right – LED intensity drift when using a current-feedback driver.

3.1.3 Prototyping

After fabrication, the components were assembled by hand for bench-testing. As these components were small and difficult to assemble, after trial-and-error I developed specific methods to ensure the device was assembled to perform as designed: the LEDs were assembled onto the miniature heat-sinks using reflow soldering as they were too small to solder by hand, and connectorized with BNC connectors for interfacing with the LED driver. The sensor cabling consisted of 2m long twisted pair wires soldered to RJ45 connectors on one end and soldered directly on to the miniature sensor board on the other end. I performed the soldering, connectorization, and wire twisting myself, as the appropriate cabling was not available commercially.

During bench-testing, recorded images showed significantly lower contrast than expected, which was traced to stray-light reflections inside of the housing. Although the housing was fabricated from black PEEK, several additional methods were tested to combat internal stray light: introducing an aperture to restrict the NA of the collector lens, using black tape to line the inside of the housing, and using commercial black paint. As illustrated in Figure 3.8, the best method to reduce stray-light was to paint the housing with high-absorption urethane-based black paint (Avian BKS, Avian Technologies LLC); this type of paint develops a microporous structure during curing, aiding in absorption of high-angle stray light.

It was also discovered that the device produced an image of the LED emitter surface at the

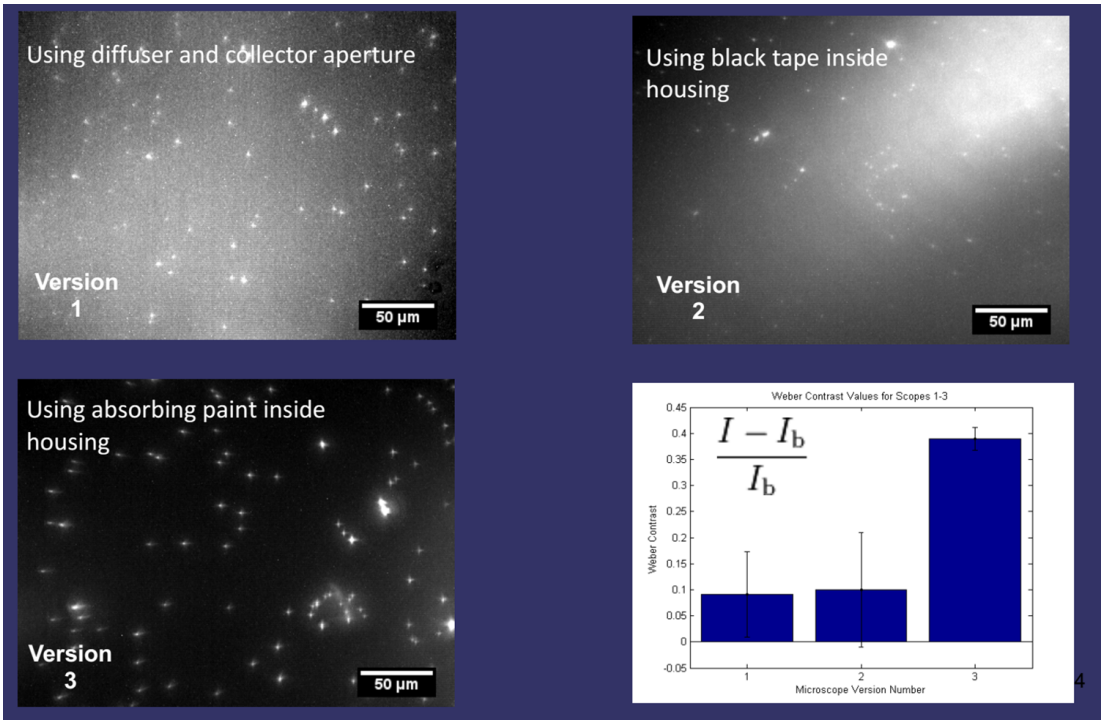

Figure 3.8: Improvements to SNR were made by elimination of internal stray-light reflections. Imaged test samples consistent of 1μm fluorescent microspheres mounted on a glass slide (F36909, ThermoFisher).

object plane, inducing a non-uniform pattern in the image Figure 3.9. To combat this, I redesigned the illumination pathway in Zemax, modifying the component spacings to correspond to a Köhler-type illumination system. A Köhler-type illumination system relays a Fourier transform of the illumination source to the object plane, which significantly improved illumination uniformity.

Additionally, it was also discovered during bench-testing that the Demo2x receiver board limited the image acquisition frame rate of the microscope to 30fps, due to the data transfer limits of the USB 2.0 protocol. Several alternatives were explored, but ultimately, this issue was resolved with the release of a USB 3.0 board a few years later (Demo3x, AGB1N0CS, Aptina Imaging Corp.).

Additionally, the biologists in the lab requested modifications to the spinal plate, which, along with the clamps, made up the spinal imaging chamber. This device was used to stabilize the spinal imaging window and to facilitate mounting of the Salk Miniscope. The original spinal plate

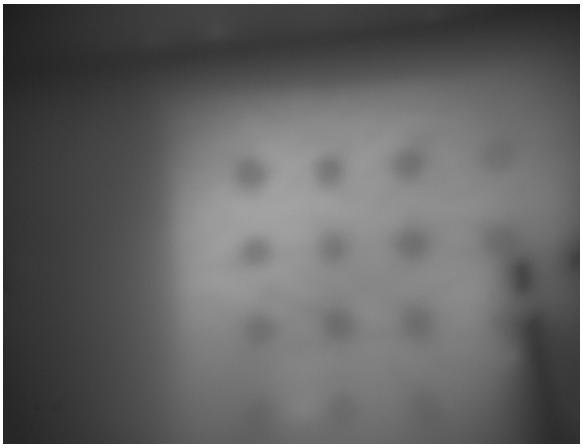

Figure 3.9: Structure of LED emitter superimposed on a uniform fluorescent image. Image taken with a fluorescence test slide (2273, Ted Pella Inc.)

was based on work from Farrar et al. [**?**]. However, as our lab wanted a larger field of view for imaging, I redesigned the spinal plate to increase the accessible field of view of the spinal window. Additionally, our lab found that when mounted over the lumbar region of the spine, the Farrar et al. spinal plate would, at times, produce pressure upon the spinal cord causing inflammation, which precluded observation of normal cellular function. To combat this, I designed the spinal plate with a concave chamfer on the bottom to conform to the shape of, and reduce sources of pressure on, the spinal cord. To date, this spinal plate design has been the preferred solution in our lab for miniature microscopy and bench-top two-photon imaging experiments. This work was performed in collaboration with, Kohei Sekiguchi, a biology graduate student in our lab.

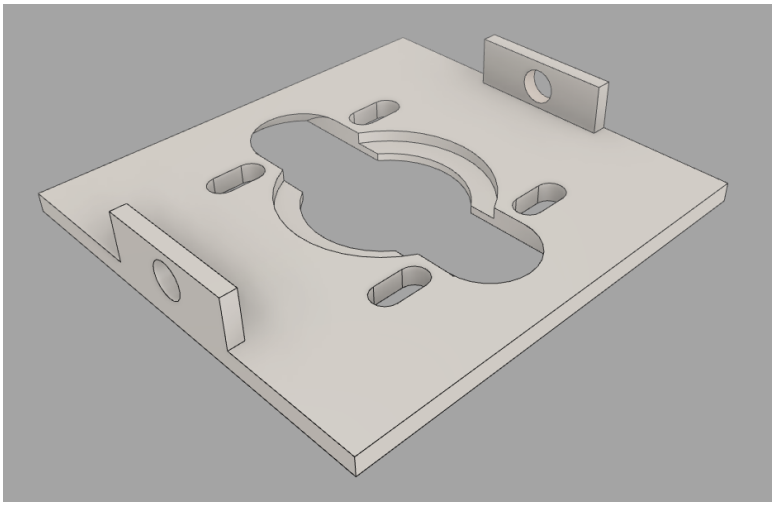

Figure 3.10: CAD design of modified spinal plate, currently in use in the lab.

3.2 Integrated Device Characterization

What follows is the integrated Salk Miniscope device's characterization.

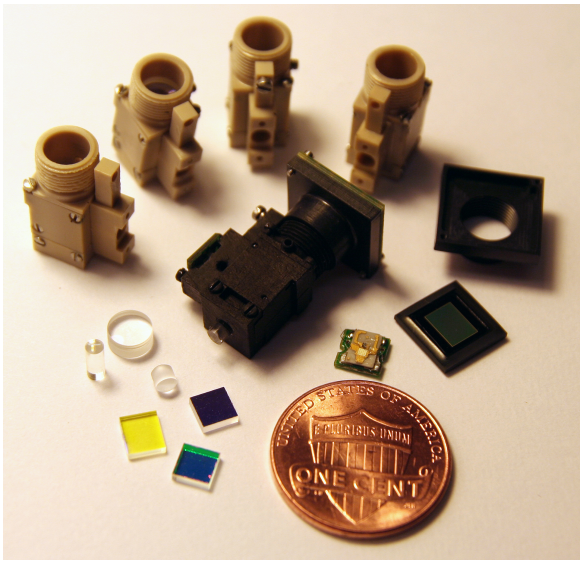

Figure 3.11: Salk Miniscope – the assembled device and the component lenses, fluorescence filters, image sensor, and illumination LED/heatsink. One cent coin shown for scale comparison.

3.2.1 Characterization Data

The salient characteristics of the Salk Miniscope device are listed in the tables below. Any deviations from the design values are discussed in the subsequent section.

Physical Attributes

Table 3.2: Salk Miniscope - Physical Attributes.

Weight	Size
2.80g	7.3 x 12.3 x 19.9mm

Optical Parameters

Table 3.3 describes the Optical Parameters of the Salk Miniscope. Table 3.4 shows the design and measured values for the magnification, FOV, and distortion of the Salk Miniscope. The magnification and FOV were measured using a grid target with 100μm spacing (Figure 3.12: B-C). Images were taken with the sensor in the middle of the focal track, and 25% from the bottom. The FOV values differed somewhat from the prediction, and the Salk Miniscope showed moderate dependence of magnification on the position of the image sensor along the focal track. Distortion was measured using the same images of the grid target, and calculated as 1.07% and 1.1%, depending on the focal track position. The distortion values were a little larger than predicted in Zemax (Figure 3.12A). Differences from design values of FOV and distortion were also attributed to variability in the device assembly stemming from difficulty in controlling the spacing between the GRIN lens and the achromatic doublet.

Digital Quantization

Table 3.5 describes the Digital Quantization specifications of the Salk Miniscope.

Table 3.3: Salk Miniscope - Optical Parameters. FOV values were measured with image sensor in middle of focal track (top line), and 25% away from the bottom of the focal track (bottom line).

Numerical Aperture	Working Distance	Magnification	Field of View
0.47	193μm	5.07x	0.970 x 0.708mm 0.890 x 0.675mm

Table 3.4: Comparison of FOV and distortion between the Salk Miniscope design and the integrated device at the middle and 25% from the bottom of the focal track.

	Design	Integrated Device (Focal Track Middle)	Integrated Device (Focal Track 25% from bottom)
Magnification	5.07	5.05	5.33
FOV	0.947 x 0.710mm	0.970 x .708mm	0.890 x 0.675mm
Distortion	0.85%	1.10%	1.07%

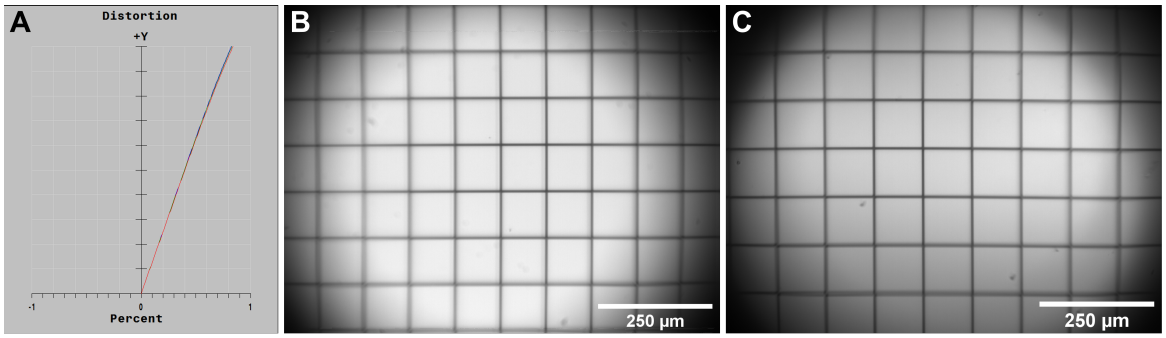

Figure 3.12: Field of view of Salk Miniscope. A) Distortion, calculated using Zemax. Images of a grid target with 100μm spacing with the image sensor positioned in B) the middle of the focal track and C) at 25% from the bottom of the focal track.

Table 3.5: Salk Miniscope: Digital Quantization.

Frame Rate	Pixel Spacing	Sensor Bitrate
45.45fps	3.75μm 0.74μm at object plane	12-bit

Imaging: Point Spread Function

Figure 3.13 shows images of the lateral and axial PSFs of the Salk Miniscope. Table 3.6 shows the lateral and axial PSF FWHM values measured using the MetroloJ plugin, along with the R^2 values of the Gaussian fit.

Table 3.6: Salk Miniscope - PSF, measured in the center of the FOV. R^2 values taken from curve-fitting results.

	FWHM	R^2
x-axis	2.468μm	0.98699
y-axis	1.969μm	0.99336
z-axis	14.047μm	0.97607

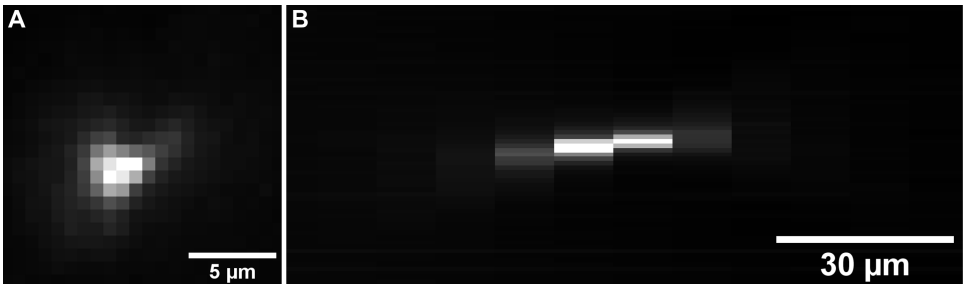

Figure 3.13: Lateral A) and axial B) PSF of the Salk Miniscope

Imaging: Limit of Resolution

Table 3.7 and Figure3.14 display the results of the LOR test at each location in the FOV. A moderate decrease in resolution is evident toward the edges of the FOV.

Imaging: Modulation Transfer Function

Table 3.8, Table 3.9 and Figure3.14 shows the results of the MTF measurements at each location in the FOV. There is a moderate reduction of contrast evident toward the edges of the

Table 3.7: Limit of resolution across the field of view

	Position in the Field of View				
	-410	-220	0	220	410
Tangential	2.27	1.25	0.91	1.67	2.27
Sagittal	1.11	0.83	1.00	2.63[1]	1.11

[1] Sagittal limit of resolution could not be determined for location (220μm, 0μm) due to severe optical aberrations. Displayed value corresponds to 4% contrast, the largest contrast value imaged

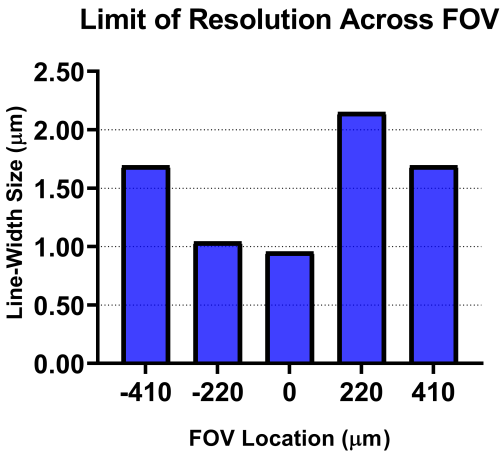

Figure 3.14: Salk Miniscope: LOR results across the FOV. Values are displayed in line-width(μm).

FOV.

Table 3.8: Salk Miniscope MTF of the integrated device computed across the FOV. Values are in lp/mm for spatial frequency.

		Position in the Field of View				
		-410	-220	0	220	410
MTF10	Tangential	160	275	328	240	217
	Sagittal	112	165	230	153	153
MTF20	Tangential	43	66	110	65	87
	Sagittal	160	275	328	240	217
MTF50	Tangential	112	165	230	153	153
	Sagittal	43	66	110	65	87

Table 3.9: MTF across the FOV converted to line-width for intuitive comparison across devices. Values are in μm.

	Position in the Field of View				
	-420	-240	0	240	420
MTF10	3.1	1.8	1.5	2.1	2.3
MTF20	4.5	3	2.2	3.3	3.3
MTF50	11.7	7.6	4.6	7.7	5.7

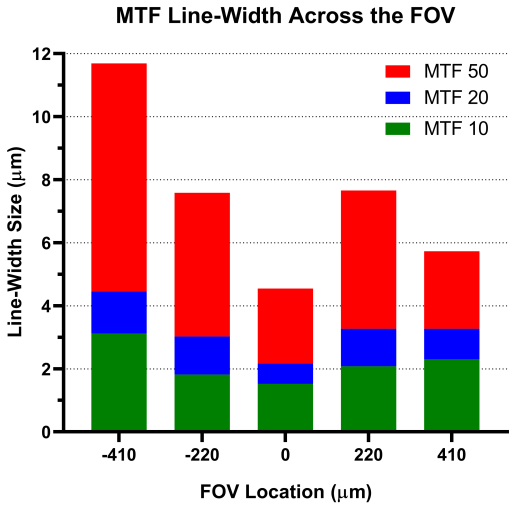

Figure 3.15: Salk Miniscope: MTF contrast across the FOV. Values displayed in line-width(μm).

3.2.2 Design vs. Integrated Device

What follows are figures and tables comparing the performance of the theoretical design with the integrated device, tested using methods described in Chapter 2. The theoretical design was evaluated in Zemax Optical Modeling Software, using the following parameters:

Where appropriate, the Zemax figures were calculated using the polychromatic condition, across λ=510-560nm, consistent with the collection band of the installed fluorescence emission filter. The wavelength components were weighted relative to the emission spectrum of GCaMP6, improving the calculated performance of the microscope relative to unweighted calculations. GCaMP6 was the primary fluorescent reporter utilized with this microscope, justifying the weighting.

Where relevant, the FOV of the Zemax figures was measured from the center (corresponding to zero on the horizontal axis), in coordinates of the rectangular image sensor: 2.4mm corresponded to the edges of the long side of the rectangular FOV, while 1.8mm corresponds to the edges of the short side of the FOV. The image sensor active area measured 4.8 x 3.6mm.

Point Spread Function

Table 3.10: Salk Miniscope design PSF compared to integrated device PSF.

PSF	Design	Integrated Device
x-axis	2.8μm	2.468μm
y-axis	2μm	1.969μm
z-axis		14.047μm

Table 3.10 and Figure 3.16 compare the measurements of the PSF with the Zemax predictions, showing good agreement. The images of the predicted PSF cross-section seen in Figure 3.16C-E display multiple central peaks, indicating some residual optical aberration. The difference between x- and y-axis FWHM of the PSF indicated the presence of astigmatic aberration, present in the measured as well as predicted results. Nonetheless, the PSF of the

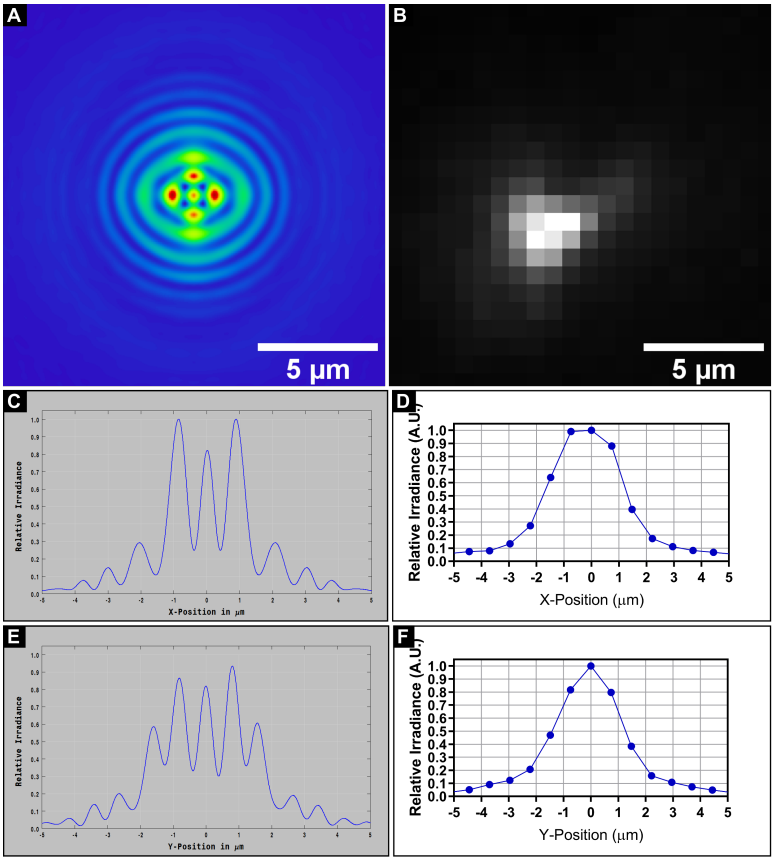

Figure 3.16: PSF of Salk Miniscope. A, C, E) Theoretical PSF, calculated in Zemax. B, D, F) Integrated device PSF. Lateral, x-axis cross-section, y-axis cross-section, respectively.

integrated device was ~3μm, a respectable result which should allow the imaging of most cell bodies and some sub-cellular processes in sparsely labeled preparations.

Modulation Transfer Function

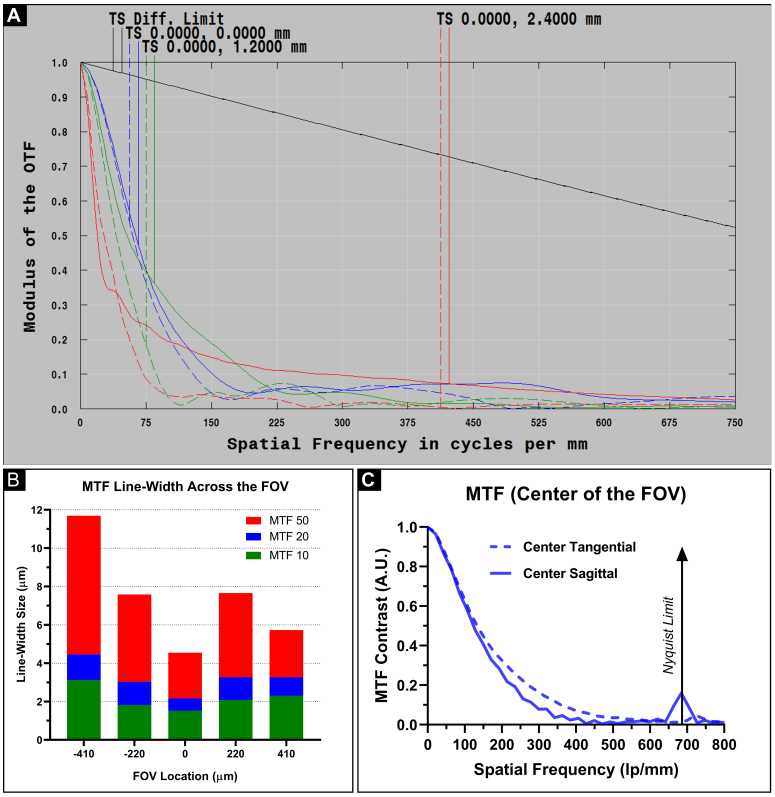

Figure 3.17: MTF of Salk Miniscope across the FOV. A) Theoretical MTF, calculated in Zemax. B) MTF10, 20, and 50 across FOV. C) Integrated device MTF in the center of the FOV.

The MTF plots (Figure 3.17) are used to characterize the contrast of the microscope. The arrow indicates the Nyquist sampling limit of the image sensor, 673lp/mm based on the pixel spacing. The microscope displayed a good MTF50 line-width of 4.6μm in the center of the FOV, but with a strong reduction in performance (~8-12μm MTF50 line-width) toward the edges. The MTF values indicated the Salk Miniscope would be able to resolve most cell bodies and a few sub-cellular processes in moderately sparse labeling environments, although less so at the edges of the FOV. Of note, comparing the predicted and measured MTF curves (Figure 3.17A, C), the MT50 spatial frequency value in the center of the FOV was ~40-50% better than predicted. I suspected this was due to a constricted aperture somewhere within the imaging pathway, likely the o-ring inserted below the image sensor in order to control stray light. Consequently, the imaging

quality of the microscope was improved, although at the cost of decreased NA and increased vignetting.

Vignetting and Illumination Profile

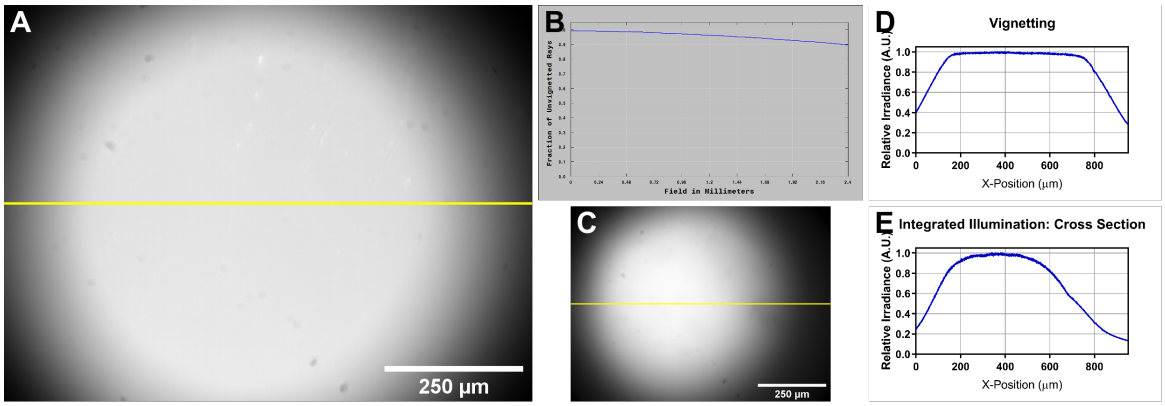

Figure 3.18: Characterization of Vignetting of the Salk Miniscope, using images of a homogeneously fluorescent test slide. A) Externally illuminated test slide, and the cross-section profile through the center D), compared to the Zemax prediction B). C) Test slide illuminated with integrated LED source and it's cross section E). Horizontal lines indicate locations of cross-section profile

Figure 3.18A shows an image of a homogeneously fluorescent test slide taken with an external illumination source to characterize vignetting in the imaging pathway (q.v. Chapter 2: Methods). The Salk Miniscope showed a remarkably flat profile in the majority of the central FOV region (panel D), owing to the aspheric index profile of the GRIN lens. However, the edges of the FOV showed a marked decrease in the image intensity, down to 0.3-0.4. This was significantly lower than the prediction of 0.9 at the edges (panel C), corroborating the presence of a constricting aperture in the imaging pathway. Panels C and E show vignetting of the integrated device, showing a further decrease to 0.1-0.2 at the edges due to the illumination pathway. The Salk Miniscope had a bright central region with strongly vignetted edges, contributing to a limited usability of the peripheral FOV regions.

3.3 Current and Future Applications

Deciphering how cellular activity in the central nervous system encodes sensory information and animal behaviour remains one of the greatest challenges in neuroscience research today. Traditionally, electrophysiological approaches have been used to sparsely sample from electrically excitable cells. Optical imaging in combination with new labelling approaches now allows minimally invasive and comprehensive sampling from dense networks of both electrically and chemically excitable cells, such as neurons and glial cells. Multi-photon imaging generally requires animal restraint, which can limit or alter animal behaviour,while miniaturized one-photon microscopy enables stable highspeed optical recording of cellular activity from superficial and deep brain regions in freely moving mice.Using the microscope that I developed, our lab demonstrated that this approach also enables stable cellular activity measurements from the spinal cord of freely behaving mice, despite the more pronounced movement of the spine within the vertebral column compared with the brain within the skull.

Using the Salk Miniscope, we showed that different types of peripheral stimuli, including tail pinch, air puff and hindquarter grooming, activate overlapping ensembles of dorsal horn neurons, and that stimulus type and intensity is encoded at the single-cell level. In contrast, astrocytes show large-scale coordinated calcium responses to intense but not weak sensory inputs. We demonstrated that stimulus-evoked calcium spiking in dorsal horn neurons is potently suppressed by general anaesthesia, and that in awake mice calcium spiking is modulated by behavioural state, akin to cortical findings. However, our lab showed that general anaesthesia also suppressed astrocyte activity in the dorsal horn, as no large-scale calcium transients were seen under general anesthesia, and unlike grey matter astrocytes of the brain, dorsal horn astrocytes also did not show large-scale coordinated calcium events triggered by locomotor activity alone. Research conducted with the aid of the Salk Miniscope resulted in a publication describing the roles of neuronal and glial cell activity in encoding sensory information in the spinal cord.

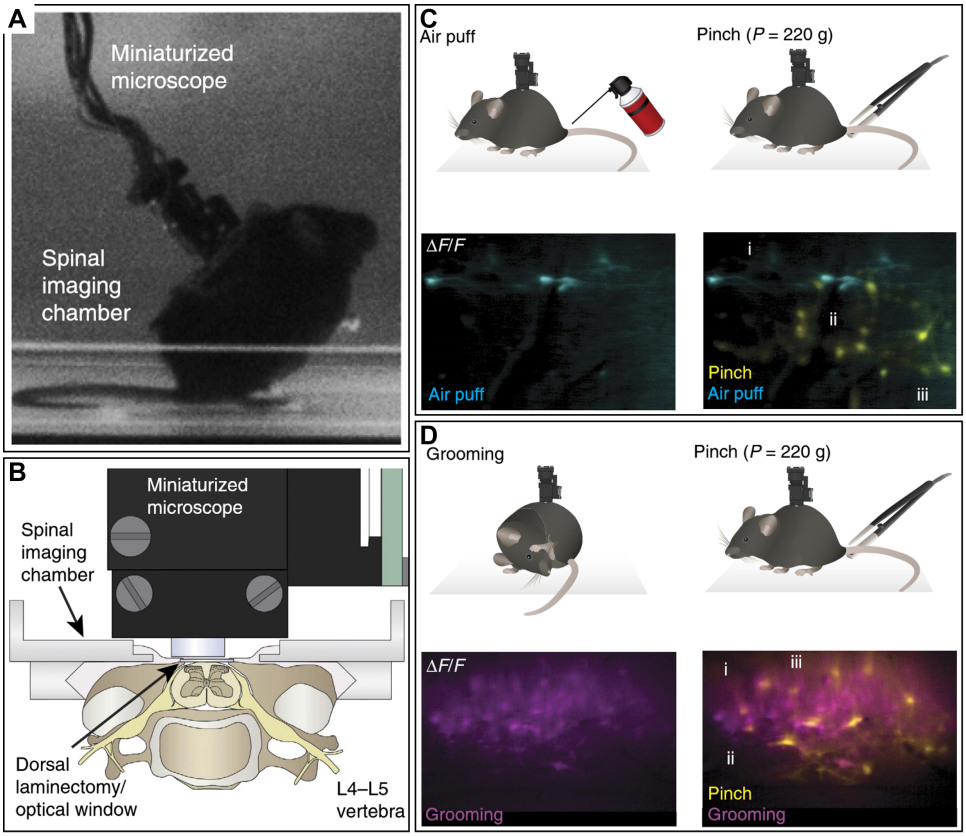

Figure 3.19: A) Image of a mouse with the Salk Miniscope mounted over a spinal imaging chamber implanted at the lumbar level. B) Schematic showing the implanted imaging chamber and mounted miniaturized one-photon microscope in cross-section. C) Top Row: Schematic of experimental approach. Two different cutaneous stimuli (pinch and air puff) were applied to the base of the animal's tail while monitoring calcium spiking of dorsal horn neurons in wild-type mice injected with AAV9-CaMKII-GCaMP6f at the L4–L5 vertebra level under unrestrained awake conditions using the Salk Miniscope. Bottom Row: Example fluorescence images showing dorsal horn neurons activated by air puff (blue) or pinch (yellow). Overlay is shown on right. Note their different spatial distribution. Three example neurons are indicated. Scale bar, 100μm. D) Top Row: Peripherally evoked calcium spiking in unrestrained awake mice (right) was compared with self-initiated hindquarter grooming near the base of the animal's tail (left). Bottom Row: Example fluorescence images showing dorsal horn neurons activated by hindquarter grooming (purple) or pinch (yellow). Overlay is shown on right. Note their different spatial distribution. Three example neurons are indicated. Scale bar, 100μm.

During the course of our in-vivo work, we observed the limitations of the Salk Miniscope. Figure 3.20 shows a comparison of images taken with a bench-top two-photon microscope (panels A-C) and the Salk Miniscope (panels D-F). The Salk Miniscope was able to resolve individual axons in the spinal cord of a Thy1-eYFP-H mouse; however, relative to the two-photon, the

Salk Miniscope produced low contrast in images of biological structures (panels D-F), as well as functional signals (panels G-H). This limited the applicability the Salk Miniscope primarily to sparsely-labeled biological environments. Consequently, one goal for the next miniature microscope design was improved contrast across the FOV.

Our work presented functional data from both neurons and astrocytes. Unfortunately, while neurons and astrocytes could be made to fluoresce in two distinct spectral bands (i.e. green and red), the Salk Miniscope could not image two distinct fluorophores concurrently due to severe chromatic aberration. As such, another goal for the next miniature microscope design was the ability to concurrently image two distinct spectral bands.

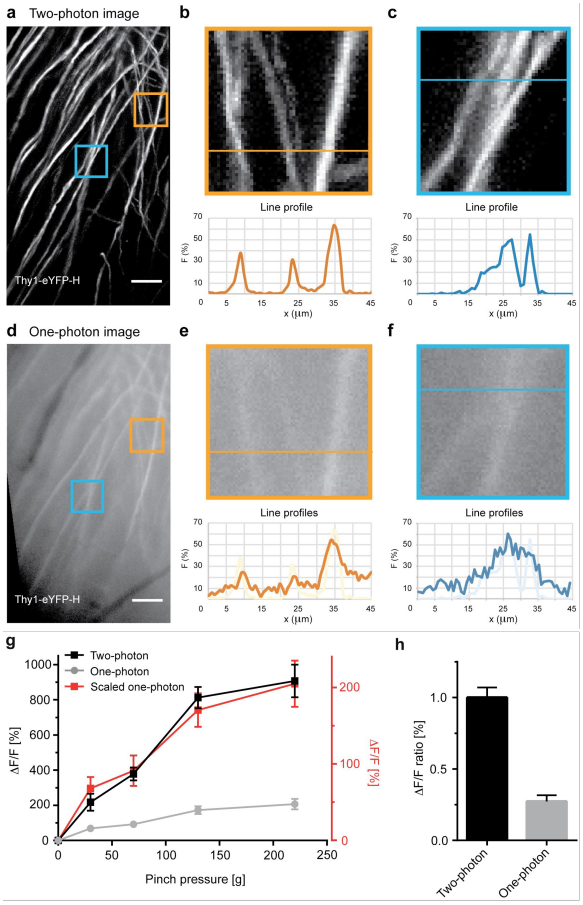

Figure 3.20: A) Maximum- intensity projection image from a two-photon z-stack (depth, 3-27μm below the dura; axial spacing, 1μm. B) Top, orange boxed region in a shown at higher magnification. Bottom, relative fluorescence intensity profile along the orange horizontal line indicated in the magnified image. C) Top, blue boxed region in a shown at higher magnification. Bottom, relative fluorescence intensity profile along the blue horizontal line indicated in the magnified image. D) One-photon volume image showing the same spinal cord region as in A. The same two ROIs as in B were analyzed. Scale bar, 50μm. E) Top, orange boxed region in D shown at higher magnification. Bottom, relative fluorescence intensity profile along the orange horizontal line indicated in the magnified image. The corresponding two-photon line profile is overlaid in light orange. F) Top, blue boxed region in D shown at higher magnification. Bottom, relative fluorescence intensity profile along the blue horizontal line indicated in the magnified image. The corresponding two-photon line profile is overlaid in light blue. Closely spaced axons or axon bundles cannot be resolved with miniaturized one-photon microscopy. G) Average pinch-evoked calcium transient amplitude as a function of pinch pressure for a representative dorsal horn neuron in an anesthetized wild type mouse injected with AAV9-CaMKII-GCaMP6f. The same cell was measured with two- (black; average power, 20 mW) and miniaturized one-photon microscopy (gray; average power, 158μW per mm^2). While both imaging modalities yield the same functional relationship (red, scaled one-photon trace), small differences in pressure amplitude can be more readily decoded from calcium transients measured with two-photon microscopy in focally restrained mice. H) Population data showing relative calcium transient amplitude of miniaturized one-photon (gray) compared to two-photon microscopy (black).

3.4 Summary

I designed and fabricated the Salk Miniscope. The microscope was small and light (2.80g, 7.3 x 12.3 x 19.9mm), with large FOV (0.970 x 0.708mm), and fast frame rate (45.45fps). The microscope showed good imaging performance in the center (2.5μm PSF, 1μm LOR, 1.5μm MTF10), and moderate imaging performance in the periphery of the FOV ($\sim$2μm LOR, 2-3μm MTF10). For the first time, a miniature microscope demonstrated imaging of the spinal cord in awake freely behaving mice. Our lab's work led to the discovery that astrocytes in dorsal horn of behaving mice showed spatiotemporal activity patterns and threshold responses remarkably different from those of dorsal horn neurons, and the description of how those signaling dynamics influence sensory-information encoding in the spinal cord. By revealing the cellular and computational logic of spinal cord networks under behaving conditions, our approach holds promise for better understanding of healthy and aberrant spinal cord processes. These neuroscientific discoveries were enabled by my work on the Salk Miniscope.

Acknowledgments

Chapter 3 contains text from a publication as it appears in Imaging large-scale cellular activity in spinal cord of freely behaving mice, 2016. Sekiguchi, K. J., Shekhtmeyster, P., Merten, K., Arena, A., Cook, D., Hoffman, E., Ngo, A. & Nimmerjahn, A. Nat. Commun. 7, 11450 (2016). The dissertation author was an investigator and second author of this paper.

Chapter 4

‘Gargantua’

Color-Corrected Miniature Microscope

The Salk Miniscope improved on the state of the art miniature microscopes available at the time. Notably, our microscope had improved sensor resolution, frame rate, light sensitivity (lower illumination power required), illumination uniformity, illumination stability, and a larger field of view (FOV).

However, our lab’s work on sensory processing in the spinal cord (Sekiguchi et al. 2016) highlighted several key limitations of our microscope. The Salk Miniscope exhibited severe chromatic aberration, and was unable to image multiple fluorophores at once, which was a serious limitation as our lab was interested in studying the interaction of neurons and glia in the spinal cord of freely behaving mice. The microscope had a short working distance (193μm), which prevented our efforts to image in the ventral motor area of the spinal cord via implantation of micro-optics, as well as made the surgical preparation of the imaging chamber more difficult to execute. Also, as Sekiguchi et al. noted, “while [the Salk Miniscope] allowed large dorsal horn areas to be monitored in freely moving mice, its limited spatial resolution and the dense labeling of astrocytes and their fine processes hampered reliable detection of astrocyte microdomain

activations". In consideration of these limitations, the following four goals were defined, in order of importance:

1. Two-color imaging: The first priority was to design a miniature microscope with the ability to image two calcium reporters emitting fluorescence in two different spectral bands.

2. Working distance: The biologists in the lab requested a larger working distance, so the goal was set to 2000μm, 10 times the working distance of the Salk Miniscope.

3. Imaging Quality: The goal was to improve on the imaging quality of the Salk Miniscope in order to be able to resolve fine structures.

4. Size and Weight: To minimize impact on experimental design, the goal was to keep the size and weight similar to that of the Salk Miniscope.

4.1 System Design

4.1.1 Optomechanics and Housing

Three distinct goals for the design of the optomechanics and housing of Gargantua were defined. The first goal was to design a housing that was small and light enough to not interfere with natural mouse behavior, yet be rigid to withstand repeated interaction with the animal while maintaining optical alignment. We chose polyether ether ketone (PEEK), an organic thermoplastic polymer, as the material of choice for the majority of the housing components. PEEK is light (density ρ=1.32 g/cm^3) yet strong (Young's modulus E = 3.6 GPa), and readily machinable. The housing components that needed to be thermally conductive were fabricated from aluminum in order to dissipate the heat generated by the image sensor.

The second goal of the design was that the housing should be easy to fabricate and assemble while maintaining optical alignment within the design tolerances. I chose 3-axis computer

numerical control (CNC) milling as the fabrication technique for the housing components. This choice dictated that complex geometry should be confined to dimensions accessible to the CNC mill. I also explored 3D printing, but after fabricating several prototype components, I determined 3D printing technology did not yet have the precision to fabricate the components we needed at that time. 3D printing materials were also found to be lacking; the plastics were either too soft or too brittle.

My final goal for the housing design was to create a modular microscope. A modular design would simplify the modification process for the microscope and additionally, would allow for extending the range of capabilities without needing to design an entirely new device. I designed the housing in Autodesk Inventor CAD software and six components – the main body, optics barrels, filters, illumination module, sensor mount, and base plate – were fabricated by Zera Development Company.

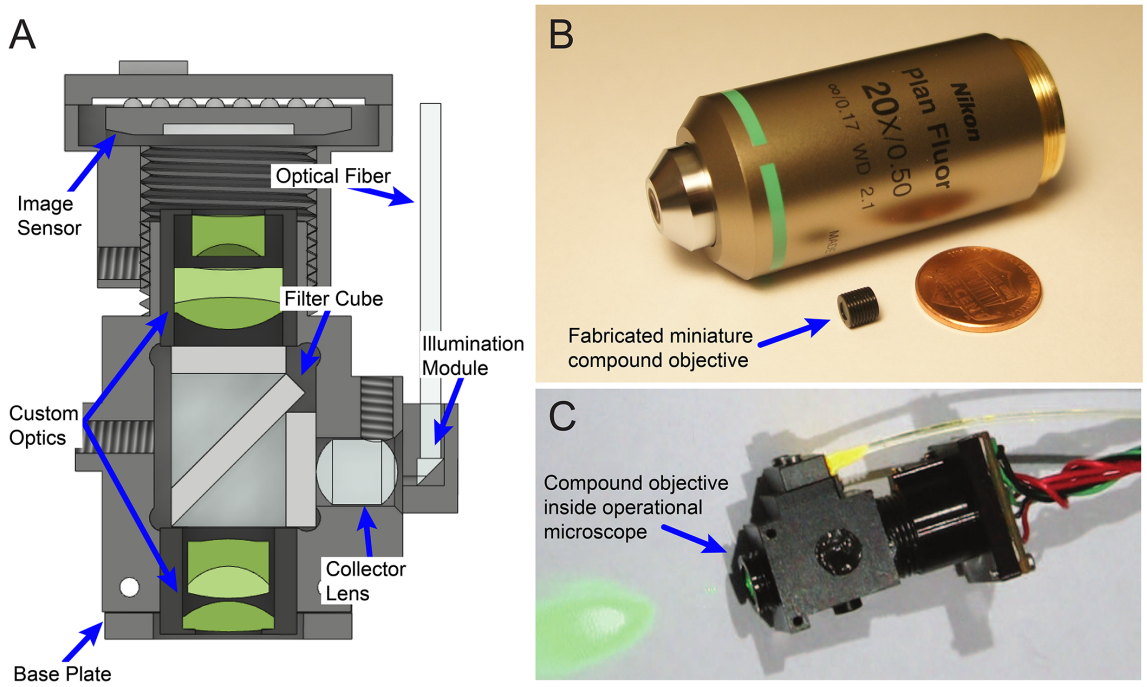

Figure 4.1: A) CAD design of Gargantua housing, optics, and filter cube. B) Objective Barrel next to standard microscope object, size comparison. C) Fabricated and assembled microscope

Main Body

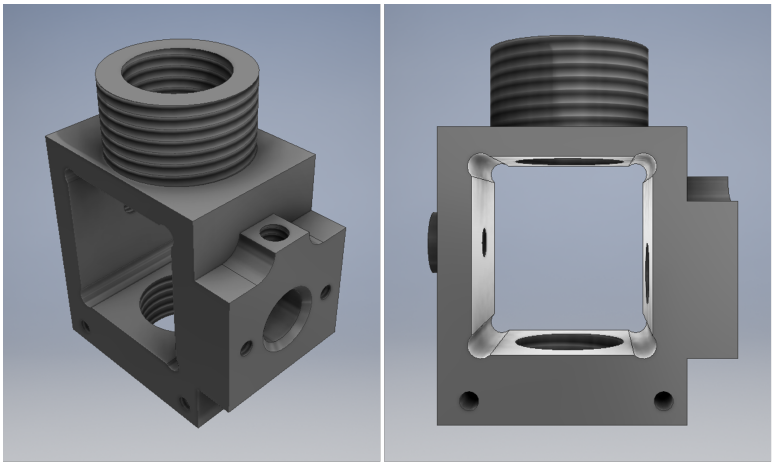

Figure 4.2: Gargantua Housing: Main Body

The main body was the central component of the housing. The main body was designed to hold the optics barrels, the filter cube and the illumination collector lens (as well as features to allow mating with the with the sensor mount), base plate, and illumination modules. I designed the housing to have an open central compartment, to allow easy access to the fluorescence filter cube during assembly, as well as to allow the exchange of filters mid-experiment.

Optics Barrels

The imaging path of the microscope consisted of six custom lens elements. The lenses required high-precision alignment in order to maintain the design performance. Drawing from my experiences with the challenges of assembling and aligning miniature components by hand for the Salk Miniscope, I designed the imaging lenses to be housed in two lens barrels, which were assembled during the fabrication process, eliminating the burden from the end-user. The two barrels corresponded to the objective and tube lens of the microscope. The lens barrels were threaded on the outside to facilitate microscope assembly by the end user. Design of the internal optomechanics and constructions of the lens barrels was performed by the lens fabrication

company, Optics Technology Inc.

Filters

In our previous microscope I found that the dichroic beam-splitters introduced aberrations due to their tilt. In that microscope's design, introducing a matching lateral offset in the optical path to correct for the one generated by the dichroic did not correct the associated optical aberrations, so I designed an all-glass filter cube configuration to address the dichroic tilt issue. Additionally, I designed the filter cube to be modular, so it could be swapped out for another filter cube mid-experiment. The filter cube consisted of the excitation and emission fluorescence filters and the dichroic beam splitter, with two fused silica prisms in between them. Fused silica was chosen for the prisms to match the substrate material of the filter. The filter cube is further described in the 'Optics' section.

Illumination Module

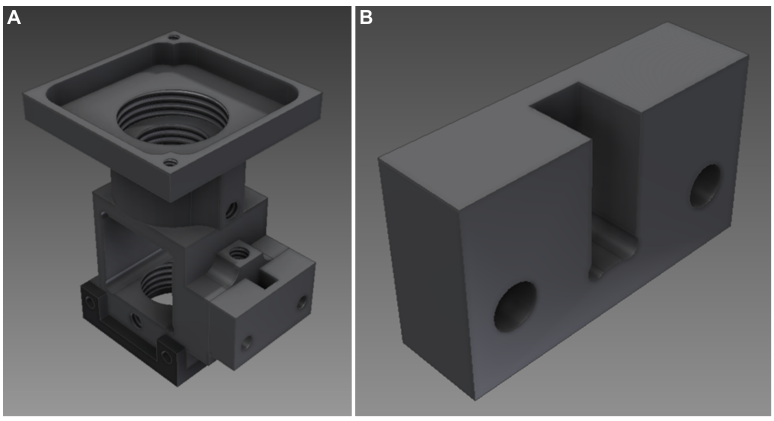

Figure 4.3: Gargantua Housing: Illumination Module 1

Rather than have one static illumination system, I designed three illumination modules, which would increase the microscope's functionality and portability. The primary illumination module, Module 1, held a vertically mounted poly(methyl methacrylate) (PMMA) multi-mode fiber (MMF) with a 750μm core and 0.51 NA, which delivered light from high intensity table-top

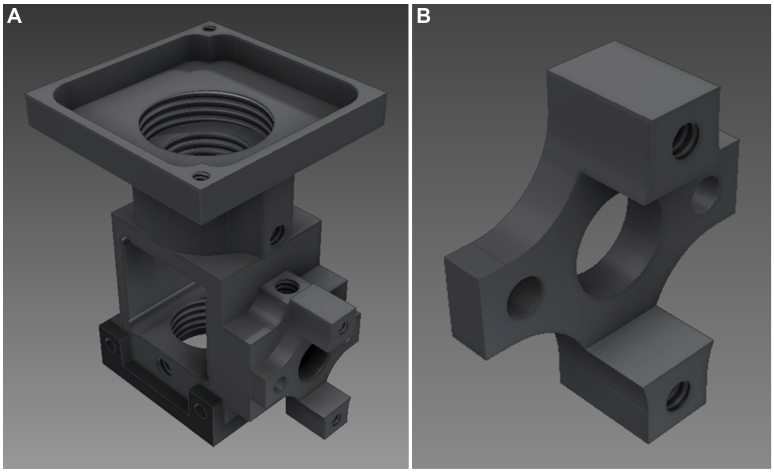

Figure 4.4: Gargantua Housing: Illumination Module 2

LED sources. A secondary, more portable illumination module, Module 2, was designed to deliver light from a miniature LED. A tertiary illumination module, Module 3, was designed for easy assembly and utilized commercial small-core MMF patch cords. Module 1 and 2 were fabricated from PEEK; Module 3 was fabricated from aluminum. The designs and applications for these modules are further described in the 'Illumination' section.

Sensor Mount

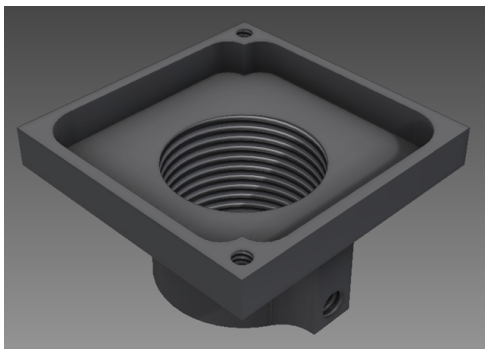

Figure 4.5: Gargantua Housing: Sensor Mount

The sensor mount was designed to hold the image sensor and associated sensor PCB board and block out stray light. The sensor mount contained threading to allow for translating

the image sensor along the optical axis relative to the rest of the microscope. This allowed for fine adjustment to focus during chronic imaging experiments. The sensor mount also contained a locking set-screw to prevent rotation after adjustment.

I chose to use the same image sensor with this microscope as we used with the Salk Miniscope, however I redesigned the sensor mount for better thermal performance. The sensor mount was fabricated from black anodized aluminum. This allowed the sensor mount to act as a heatsink for the image sensor, reducing the image sensor temperature by ~20°C, which reduced thermal noise in the sensor. Non-conductive thermal transfer tape was used to non-permanently mount the image sensor board to the sensor mount.

Base Plate

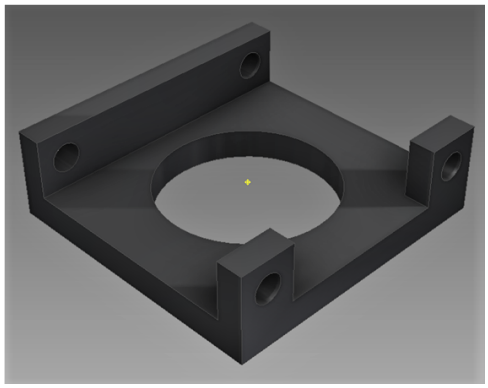

Figure 4.6: Gargantua Housing: Base Plate

During live animal imaging, the microscope was mounted onto a cranial or spinal plate, which stabilizes the surgical preparation of the imaging window in the brain or spinal cord, respectively. The baseplate was designed to facilitate chronic imaging experiments. During the mounting procedure, the microscope was secured to the spinal plate. At the end of each day's experiments, the microscope was detached from the baseplate, leaving the baseplate attached to the animal. Thus, when the experiments were resumed at a later day, the procedure to mount, align, and focus the microscope was greatly simplified.

4.1.2 Optics

The goals for the optical system design of Gargantua were to match or exceed the performance of the Salk Miniscope. The design specifications I focused on were numerical aperture (NA), magnification, optical track length, working distance, resolution, and achromatic wavelength range.

As can be seen in Table 4.1 below, the goals for the numerical aperture (NA), magnification, and optical track length were to match those of the Salk Miniscope. The goal for the working distance (WD) was to increase the Salk Miniscope's 193μm distance. The biologists in our lab requested a longer WD since at times, surgical preparations would have to be redone. The surgery was challenging – it required the elevation of the spinal cord relative to the spinal vertebrae, and the short WD of the Salk Miniscope left a very small margin for error. The goal for the resolution was to increase the performance both in the center and across the field of view (FOV), especially since the Salk Miniscope's resolution degraded by up to four times at the edge of the FOV. Lastly, the specification 'Achromatic Wavelength Range' (AWR) was added to the design goals. I defined the AWR goal based on the emission spectra of the available fluorescent calcium reporters (GCaMP6 and RCaMP/jRGECO).

Table 4.1: Design goals for Gargantua compared to the Salk Miniscope's Zemax design.

Specification	Salk Miniscope (Actual)	Gargantua (Goals)
Numerical Aperture	0.47	0.47
Magnification	5.07	5.00
Optical Track Length	~20mm	20mm
Working Distance	190μm	2000μm
RMS Spot Size - Center	4μm	$\leq 4\mu$m
RMS Spot Size - Edge FOV	15μm	$\leq 4\mu$m
Achromatic Wavelength Range	-	500-620nm

Imaging Path

The optical design was performed using Zemax optical modeling software and manual calculations. During the design phase, geometric distortion was deliberately allowed to increase to 5.7% in order to gain improvement across the other Seidel aberrations (spherical, coma, astigmatism, and field curvature). First, paraxial equations were used to create a general design form. The starting point for this design was based on the Biotar type Double Gauss photographic lens, although my design went through significant revisions during the optimization process. The Double Gauss was selected for it's high NA and good performance across a large FOV; it was then modified based on my paraxial calculations, and optimized using the "Local Optimization" function in Zemax, to create a realistic design using spherical lenses. Spherical lens elements were selected, and exotic glass materials were avoided, to simplify fabrication. The "Hammer Optimization" function was then utilized until significant changes to the merit function were no longer observed (between 24-72 hours). The design was then modified using perturbation-optimization, which consisted of manually perturbing the design and merit function parameters and performing aggressive local optimization in an attempt to coax the design out of any local minimum. The "Hammer Optimization" and perturbation-optimization two-step process was repeated recursively, and, along with the evolving design, significantly novel designs were manually saved in a design library for further exploration. 'Novelty' was based on optical performance, perceived optimization potential, and fabrication feasibility. These novel designs were then processed repeatedly through the recursive two-step process, which was discontinued when the "Hammer Optimization" step yielded the same results as the previous round.

The initial prospective designs were formalized by setting the following parameters based on the design goals: track length, NA, magnification, and field of view (based on the size of the image sensor). Ray bundles (i.e. bundles of rays origination from a single point within the FOV) were constrained to be near-collimated in the filter space. The two halves of the optical system

around the fluorescence filters were optimized independently. Between the two halves was the conjugate space necessary for correct operation of the fluorescence filters; the length of the was set to be slightly more than twice the aperture stop diameter.

In the later stages of the design process, the two halves of the optical system were combined and optimized together. Optimizing the two halves together expanded the optimization search space and allowed the optical system to have better performance (particularly in regards to color-correction), without affecting the performance of the fluorescence filters. However, this design choice also led to higher sensitivity to misalignment in the filter space, which became apparent after the fabrication process and is discussed further in the section below "Post-Fabrication Modifications".

The design went through approximately 75 iterations before the final design was set.

Tolerance analysis for fabrication was performed in Zemax using the Monte Carlo Analysis. Tolerances were set to "loose", and were tightened until the RMS spot radius and wavefront error at 90% yield met the performance goals. The final optical design utilized six lens elements, each designed with a different glass material, all fabricated by Optics Technology Incorporated. The lenses were housed in two separate barrels (Optics Technology Inc.) that were joined with a filter cube element.

Figure 4.7 shows the optical layout of the finalized Gargantua design. Tracing the marginal and chief ray through the lenses defines the Lagrange invariant, which is sufficient to characterize the imaging properties of an idealized (i.e. minimally-aberrated axially-symmetric) optical system. Figure 4.8 shows the optical prescription of Gargantua.

Filter Cube

Like the Salk Miniscope, Gargantua was based on the epifluorescent wide-field configuration. When considering an epifluorescent wide-field configuration, it was important to note the limitations in regard to miniaturization. In a typical epifluorescent wide-field configuration, the

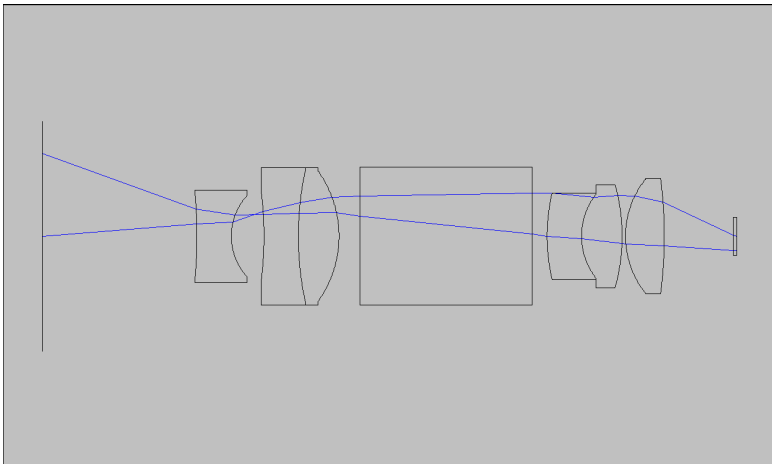

Figure 4.7: Optical layout of the finalized Gargantua design. Rectangular region in the center represents the all-glass filter cube. The two rays traced through the lens system represent the chief and marginal rays

Surf	Type	Radius	Thickness	Glass	Diameter
OBJ	STANDARD	Infinity	0		6
1	STANDARD	Infinity	4.5		4.8
2	STANDARD	-13.65635	1	N-SF57	2.679
3	STANDARD	1.758689	0.9479822		2.349
4	STANDARD	-10.38426	1	N-BALF5	2.657
5	STANDARD	9.049044	1.182136	N-LASF40	3.988
6	STANDARD	-3.253426	0.6096153		3.785
7	STANDARD	Infinity	5	F_SILICA	4
8	STANDARD	Infinity	0		4
9	STANDARD	Infinity	0.4398171		2
STO	STANDARD	5.543071	1	N-SF66	2
11	STANDARD	1.973004	1.177709	N-PK51	1.991198
12	STANDARD	-5.628253	0.1		2.994
13	STANDARD	2.635428	1.127833	N-LAK34	3.297
14	STANDARD	-13.04288	2		3.36
15	STANDARD	Infinity	0.1	D263M	0.8690751
IMA	STANDARD	Infinity			0.8293949

Figure 4.8: Optical prescription of Gargantua

fluorescent emission light is collimated when passing through the dichroic beam-splitter. When a collimated beam is passed through a tilted glass plate, a lateral offset is introduced into the light path. Therefore, the optical system loses axial symmetry, and on-axis astigmatism is introduced. The amount of offset is proportional to the thickness and refractive index of the dichroic substrate. If the light beam is converging or diverging, chromatic aberration is also introduced, proportional

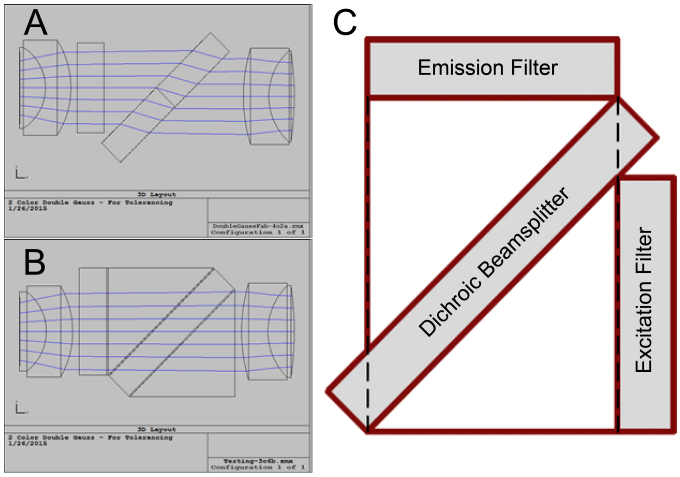

Figure 4.9: Gargantua Filter Cube. A) Effect of dichroic tilt on miniature form-factor imaging optics. B) Index-matched prisms eliminate effective tilt. C) Current geometry of filter cube.

to the amount of deviation from the collimated condition.

In a typical table-top epifluorescent system this offset is minor, as the collimated beam diameter is large in relation to the dichroic thickness: ~25mm and ~1mm for our lab's tabletop microscope, respectively. Miniature epifluorescent microscopes have a smaller beam diameter relative to the dichroic thickness: 2mm and 1mm for the Salk Miniscope, respectively. This means the corresponding astigmatism is larger, and causes miniature epifluorescent microscopes to have degraded imaging quality in comparison to tabletop epifluorescent microscopes. Additionally, introducing a matching lateral offset in the optical path to correct for the one generated by the dichroic, as done in the Salk Miniscope, does not correct the associated optical aberrations. In the end, an all-glass filter cube configuration was selected and designed to address the dichroic tilt issue, as illustrated in Figure 4.9. Using an all-glass filter cube eliminates the astigmatism created by a tilted dichroic because the light passes through all glass-air interfaces normal to the interface plane.

A few approaches were considered during the initial design phase. The first was the use of a standard filter configuration with a thinner dichroic substrate. I initially designed a filter cube

with fluorescence filters consisting of thin film coatings deposited directly onto the faces of two prisms glued together into a cube, however, at the time this design was found to be prohibitively expensive to fabricate. A dichroic on a 0.2mm substrate was used in a recent miniature 2-photon device [6] (published after the fabrication of this microscope was completed), though this is typically not available with off-the-shelf dichroic beam-splitters. A second method considered was to use a pellicle-membrane dichroic beam-splitter, as the substrate thickness is on the order of a few micron, however, I could not find any wavelength-selective pellicle beam-splitters available for sale. Another method to correct for astigmatism by incorporating cylindrical or non-spherical optics into the design was considered, but ultimately was not utilized as there was not enough space for individual cylindrical optics within the design, and creating non-axially-symmetrical lens elements was considered prohibitively expensive.

The first filter cube fabricated consisted of fluorescence filters in a commercially available form factor. During bench-testing, this filter cube geometry was found to introduce color-shifts at the edges of the field of view. To address this, another iteration of the filter cube consisted of modified geometry was fabricated, eliminating the color shift at the FOV edge. This lengthened the optical path between the barrels beyond the design tolerance, introducing optical aberrations due to the filter space being longer than design tolerances. In order to eliminate these aberrations, I constricted the aperture stop by placing a narrower retainer ring into the barrel, reducing the device NA from 0.46 to 0.41, which led to a 21% decrease in light collection. During assembly of the microscope, the filter cube was secured in place by the optics barrels, each applying a force on the filter cube from opposite directions. The edges of the barrels, at the interface with the filter cube, were sealed with an opaque absorbing silicone.

Unfortunately, after the lens system was fabricated, it was discovered that the filter manufacturers mis-calculated the feasibility of using their stock filters in this configuration. Because of this, a custom dichroic coating had to be designed and fabricated. The stock 59012bs dichroic beam-splitter was designed for 45-degree incidence from air, so a custom coating that

matched the 59012bs transmission spectrum was manufactured so the filter could be used for a 45-degree incidence from glass. Unfortunately, this custom dichroic reduced the light-collection efficiency and introduced stray-light reflections, both of which contributed to diminished signal to noise, leading to lower contrast and sensitivity of the device.

The final filter cube consisted of dual-band excitation and emission fluorescence filters (59012x and 59012m, Chroma Technology Corp.), a dichroic beam splitter (59012-custom, Chroma Technology Corp.), and two fused silica prisms (Tower Optical Corp.) in between. The dual-band fluorescence filters were chosen to match the spectra of the calcium reporters GCaMP and RCaMP, and were cut to custom sizes. The filter cube was assembled in-house with index-matched UV-cure adhesive (NOA146H, Norland Products Inc.) to minimize internal reflections, and the outside was painted with a custom black paint (black pigment dispersed in NOA146H, Norland Products Inc.) to absorb stray light reflections. Figure 4.10 shows transmission spectra of 59012m/x/bs (panel A) and custom dichroic 59012-custom (panel B). Transmission spectrum of 59012-custom was measured in lab with a fiber spectr-photometer.

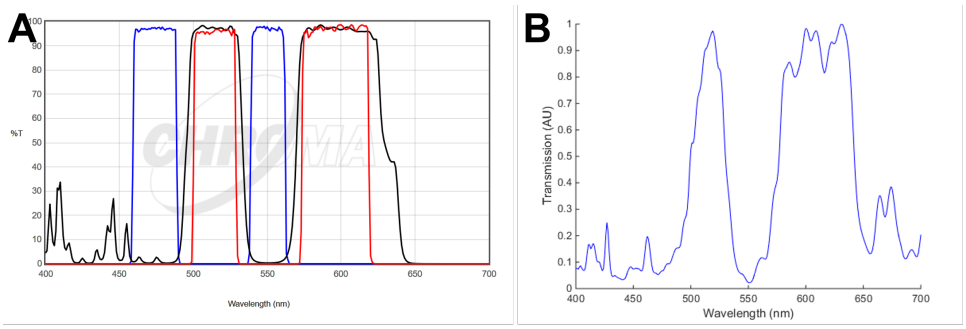

Figure 4.10: Comparison of transmission spectra of stock and custom dichroic beam-splitters. A) Stock dichroic beam-splitter 59012bs (black trace), Chroma Technology Corp. B) Custom-coating dichroic beam-splitter (blue trace).

4.1.3 Illumination

In order to meet the device goal of concurrently observing multiple fluorescent reporters, the illumination system's goals were to deliver multiple spectral bands to the tissue being imaged.

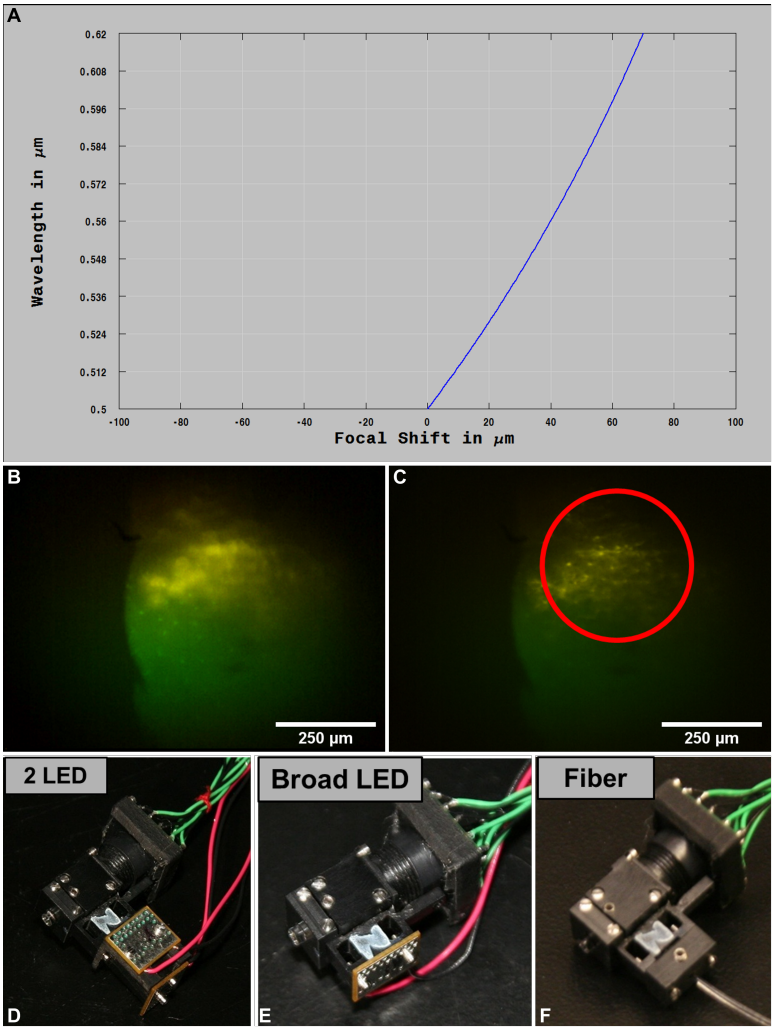

Figure 4.11: Axial Chromatic Aberration of the Salk Miniscope. A) Chromatic focal shift, calculated in Zemax. B-C) Images of tissue slice with two cell types labeled with different spectral emission bands B). D-F) Prototypes build to investigate three approaches to delivering multi-spectral light

A secondary goal was to perform optogenetic manipulation using one spectral band, while imaging in another spectral band. Unfortunately, while neurons and astrocytes could be made to fluoresce in two distinct spectral bands (i.e. green and red), the Salk Miniscope could not image two distinct fluorophores concurrently due to severe chromatic aberration (Figure 4.11: A-C). Consequently, another goal for the Gargantua design was the ability to concurrently image two distinct spectral bands.

Illumination of the tissue with multiple spectral bands of light is desirable during multi-color imaging, as each fluorescent reporter had a distinct absorption spectrum. Optimizing the illumination spectrum to match the absorption peaks of each fluorophore maximized the fluorescent-signal emission while minimizing photo-damage induced at the tissue. Independent control of the intensity of each excitation band allowed for matching the emission intensities of the fluorophores. A device capable of delivering multiple spectral bands of light to the tissue also enabled concurrent optogenetic manipulation at the imaging site, within the same device.

Though the Salk Miniscope was unable to image multiple spectral bands, the design work for multi-band light delivery began with one of the prototypes (Figure 4.11). The Salk Miniscope was used as a test-bench for three approaches to delivering multiple spectral bands of light to a miniature microscope (Figure 4.11: D-F). The first prototype (panel D), which integrated multiple miniature LEDs into the microscope, had the advantage of low cost and portability. However, this configuration had low throughput from the LEDs, requiring high drive current and causing the device to increase in temperature. This increase in temperature had the potential for heat damage to the animal and drift (dimming) of the LEDs. Additionally, scalability was an issue, since each additional LED, and corresponding coupling optics, would add weight and size to the device. The second prototype utilized a broadband LED (panel E). This method was found to be impractical, as it was not possible to control the intensity of each spectral band independently.

The third prototype tested utilized an optical fiber (panel F). The main advantage of this method was the reduction of the amount of illumination intensity lost to stray light, due to the small NA of the fiber face relative to an LED emitter. Other advantages included: maintaining device weight and size independent of the number of light sources, the ability to use bench-top light sources such as high-powered LEDs and narrow-band lasers, precise control of the spectra of each light source with multiple single edge spectral filters, and the potential to utilize off-the-shelf fiber parts to simplify the process of wavelength multiplexing. However, this method was found to have some limitations: the limited launch-coupling efficiency from large-area LED emitters,

potential for loss of portability due to the size of the table-top fiber-launch setup, and the potential for speckle if a laser were used.

These prototypes directly helped to inform my design decisions for Gargantua. At the time of the design phase, there were no publications or devices that could deliver multiple spectral bands with the ability to image at least one color, hereto referred to as 'concurrent optogenetics'.

Illumination Delivery

Delivery of illumination light via fiber-optic cable (panel F) was ultimately deemed the preferred solution, as weight and size, scalability, and stray light control were a priority. A fiber-optic light-delivery system could leverage a variety of incoherent and coherent bench-top light source, and could scale to larger numbers of spectral bands without the addition of extra components to the miniature microscope package. This prototype was tested for concurrent in-vivo imaging and optogenetic manipulation (as light-based activation of opsins does not require color-corrected optics). An added benefit of this method was that it allowed for a modular design of the illumination system. A modular design allows for greater ease of repair and the implementation of upgrades. Lastly, using a fiber simplified the illumination optics on the device-side because the light source at the integrated device end is well-characterized.

Illumination Module 1 : Primary

I designed three separate illumination modules to increase the portability and functionality of the device. The primary module used a poly(methylmethacrylate)-core (PMMA-core) multi-mode fiber (MMF) with 735μm core and 0.51 NA (Eska, Mitsubishi International PolymerTrade Corp.), and utilized two high intensity table-top LEDs as the illumination sources. The large core-size and NA facilitate efficient light coupling from the extended emitter area of the LED (1mm^2). And though traditionally MMFs are silica-core-based, I selected a PMMA-core MMF since its flexible properties aided the animal's mobility.

The primary illumination module was also routinely used with two table-top laser sources for optogenetic experiments. The lasers were because the illumination intensities required were higher than what the LED's could provide. The MMF was connectorized and polished on one end, and bare-end polished on the other end. Robert Folk, one of our lab technicians, performed all the MMF polishing and connectorizing work for this project.

This illumination module also included a 1.4mm 45° fold-mirror, constructed from two 45°-45°-90° reflective-coated prisms (Tower Optical Corp.) which were glued at the hypotenuse to form a glass 1 x 1 x 1mm cube, and mounted inside the illumination module and coupled to the optical fiber using index-matched UV-cure adhesive (NOA81, Norland Products Inc). The collector lens was secured inside the main body. This module allowed the MMF to be vertically coupled to the horizontal collector lens (Figure 4.1). I intentionally designed this module for vertical MMF mounting since we had previously observed animals scratching and chewing the fiber, attempting to climb the fiber length, and getting tangled in the fiber, when working on the optogenetic-enabled Salk Miniscope prototype. The illumination optics consisted of one collector lens. The collector lens, used in conjunction with the objective barrel, projected the coupled illumination light onto the tissue. I used a high-index flint-glass drum lens (45-664, Edmund Optics) as the collector lens.

Illumination Module 2

Module 2 was designed to meet the need for portability. The lab wanted to loan out the microscope, but Module 1 was designed to work with our table-top fiber-launch setup that could not be moved. I designed Module 2 to work with the miniature LED and driver from the Salk Miniscope since we had additional units. The LED is coupled to Module 2, which is then mounted directly behind the horizontal collector lens. No fibers are used.

This secondary module design cannot be used for optogenetic experiments or multi-color imaging, but is very affordable/cost-effective and allows our collaborators to image with

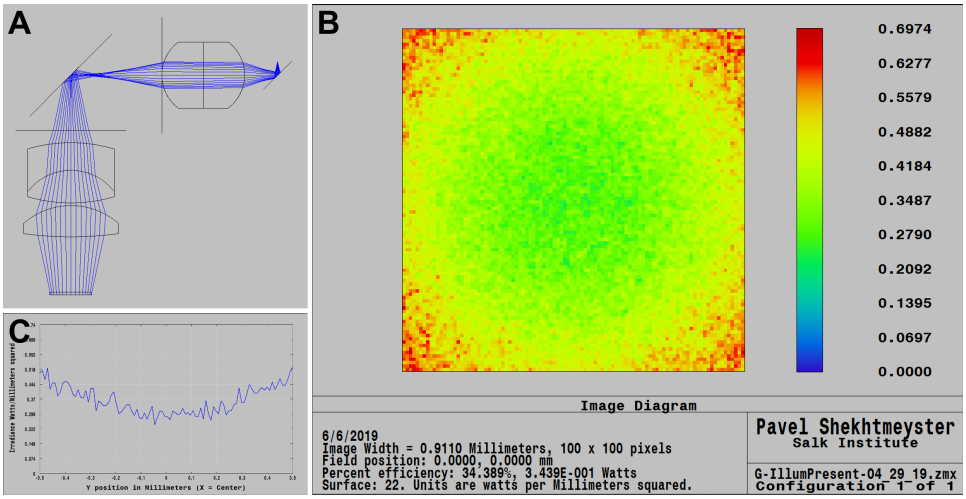

Figure 4.12: Illumination Module 1. A)Illumination pathway for module 1 B-C) Uniformity of illumination and efficiency of light delivery

Gargantua's high-resolution optics in situations where the cost and time investment of a table-top fiber-coupling setup is undesirable.

Illumination Module 3

Module 1 was hand-assembled. This process included MMF polishing, connectorization, and fold-mirror alignment and integration. This was a very difficult and time-intensive process, so a third module was designed in hopes of utilizing stock components and minimizing in-house processing.

I designed the tertiary illumination module for mating with silica-core MMF patch cords, which eliminated the need for polishing and connectorizing. Since silica-cores are more rigid, I used a 240μm core MMF with a fiber buffer (Eska, Mitsubishi International PolymerTrade Corp.), connectorized with an SMA connector on one end and 1.25mm diameter ferrule on the other end. The original design's collector lens was removed and replaced with a 1mm sapphire ball lens (#43638, Edmund Optics). Unfortunately, Module 3 must be used exclusively with table-top laser sources, as the MMF core-size was too small to efficiently couple light from our table-top LED launch setup.

Light Source

The first multi-spectral table-top light source fiber launch layout was drawn by hand and tested via the optogenetically-enabled Salk Miniscope prototype. When building the Salk Miniscope prototype, blue (470nm) fiber-coupled LED packages (M470F1 ThorLabs) and mounted LED packages (M470L1 ThorLabs) were commercially available. Yellow (565nm) LEDs were not available in any mounted form, and yellow lasers were prohibitively expensive. A yellow unmounted SMT package (MINTL5, ThorLabs) was purchased and soldered onto the same model printed circuit board (PCB) as used for the Salk Miniscope LED light source. The PCB was then thermally coupled to a large heat sink, and then I hand-polished an MMF before butt-coupling it to the LED emitter. The output of the MMF was launched into free-space where it was combined with blue LED output, then launched into a secondary MMF, which was coupled into the Salk Miniscope prototype. This layout, while functional, was not ideal as it was not portable, not shielded, was prone to melting, and extremely difficult to be operated and aligned with precision and accuracy because of the manual assembly required. Different components were tested to make alignment easier and more precise while ensuring maximum output power coupling efficiency.

The final layout design consisted of blue (470nm) and yellow (554nm) mounted LED packages (M470L4 and MINTL5, Thorlabs) combined in free-space, coupled into a silica-core intermediary MMF patch-cord (M59L01, ThorLabs), which was then mated to the Gargantua Module 1 MMF using an SMA to SMA Mating Sleeve (ADASMA, ThorLabs). Using the intermediary MMF patch-cord allowed for the precise alignment of the LEDs to be unaffected when switching Gargantua's light source (i.e. when switching between the LED and laser light sources).

4.1.4 Electronics

Optical imaging of multiple spectral bands required one of several multiplexing schemes at the image sensor. Gargantua was designed with an RGB image sensor to record multiple spectral bands.

Temporal multiplexing was tested with the optogenetically-enabled Salk Miniscope prototype's monochrome image sensor (see Figure 4.11). It was the simplest implementation using the available hardware. The light sources were temporally modulated so that each imaging frame was illuminated with by a single spectral band, and the interleaved spectral bands were recorded. Long recordings were unsuccessful due to hardware limitations, as the light sources were not able to be stay synchronized with the detector frame rate, causing the light sources to drift out of alignment relative to the recording, which generated imaging artifacts. Short recordings of multiple spectral bands were successful, and were converted into digital color-channels by deinterleaving. Unfortunately, the converted recordings exhibited cross-talk between the different color-channels, because the two fluorescent reporters had overlapping absorption spectra and were excited by the same illumination spectral band. For example, in our lab we used GCaMP6, a green calcium reporter, and tagRFP, a red structural-indicator. At GCaMP6's 100% absorption efficiency wavelength of 497nm, tagRFP was also excited at an absorption efficiency of ~30%, causing both to fluoresce at the same time. Additionally, the genetic expression specific to the individual animal was a source in variability. This cross-talk was able to be resolved by performing a calibration step using still images of two reference fluorescence samples used to define the digital color-channels. However, this proved to be inefficient as it was greatly time-consuming and needed to be repeated any time the brightness of the illumination changed, or a new experiment was performed. Due to these limitations, three additional multiplexing schemes were explored.

Spatial multiplexing, which required a spatial tiling of individual single-band spectral

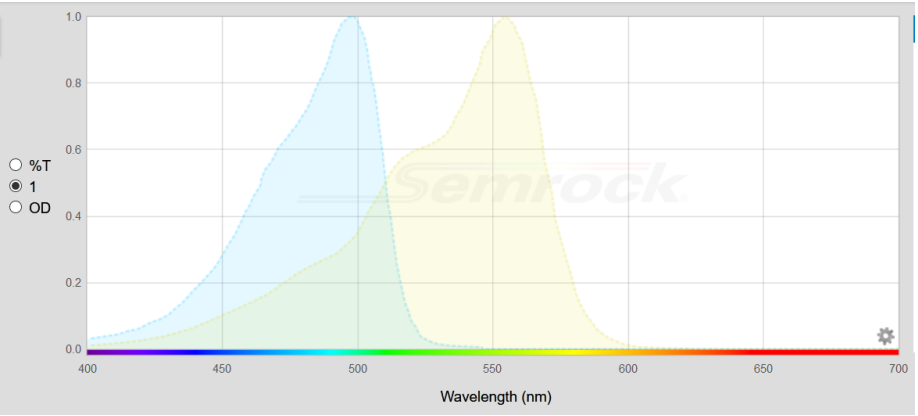

Figure 4.13: Absorption Spectra of GCaMP6 and tagRFP. Generated using SearchLight tool, courtesy of Semrock.com.

filters corresponding to each color channel along with a single monochrome image sensor, was considered. This approach was rejected as it compromised the FOV, required additional optics, and increased the complexity of fabrication and assembly. The multi-sensor approach was also explored as it preserved resolution and frame rate. This method utilized a dedicated image sensor for each color-channel, eliminating the need to compensate for axial chromatic aberration of the imaging optics. However, this method was also rejected as it increased the size and weight of the device, and was difficult to scale above two spectral bands.

The RGB sensor multiplexing scheme was determined to be the best for the following reasons: 1) FOV and frame rate of the Salk Miniscope were preserved; 2) It was easy to scale to three colors; and 3) while there was some potential for a small reduction in resolution, it was believed this could be largely mitigated by demosaicing algorithms which were widely available, well-researched, and robust. Aptina's RGB Model-MT9M024 sensor was selected for the final design.

Gargantua utilized the same custom sensor board model as the Salk Miniscope, which had been designed in collaboration with by Axelsys. The boards were fabricated and assembled for project by Advanced Assembly Inc . Gargantua utilized the Demo3 USB 3.0 receiver board and HiSpi adapter board (AGB1N0CS and AGB2N0CS respectively, Aptina Imaging). The sensor

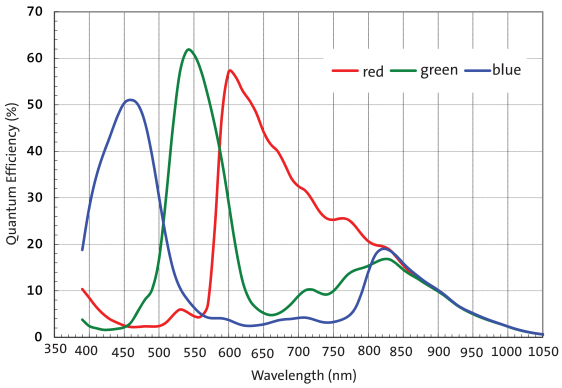

Figure 4.14: Estimated quantum efficiency of MT9M024-RGB image sensor, and its constituent color channels

control and image acquisition were performed using the Aptina DevWare Software. I wrote custom register-control scripts to automate the sensor start-up and also added gain functionality not available in the generic software package.

Sensor Electronics and Control

The electronics design was identical to the Salk Miniscope. At the time, no significantly better-performing sensor was available ('better performing' was defined as greater than 5% higher resolution while maintaining the same sensitivity), so the same sensor model was used (Model-MT9M024, Aptina Imaging). Since the same sensor board was used, the data-acquisition board, the cabling design and connectors, and the sensor control software also stayed the same. The only change was the replacement of the monochromatic image sensor chip with an RGB CMOS sensor, chosen for its high-sensitivity (5.48V/lux-sec), resolution (1280x960 pixels, 0.69μm spacing at object plane), and frame rate (45 fps) (MT9M024IX3STC, Aptina Imaging). The sensor was mounted on a custom miniature printed circuit board (PCB) and was interfaced with an Aptina data-acquisition board (AGB1N0CS-GEVK), and was controlled using the Aptina DevWare Software Package.

For the purposes of this discussion, the fluorescence emission is referred to as 'spectral

bands', and the digitized color-information is referred to as 'color-channels'.

Cabling and Connectors

Unlike the Salk Miniscope, the twisting of wire pairs for the sensor cabling was outsourced to Advanced Assembly Inc. This was hugely beneficial as it was much faster and more precise than twisting by hand. The sensor cabling connectorization for Gargantua was completed by our Lab Technician, Chelsea Jan.

4.2 Integrated Device Characterization

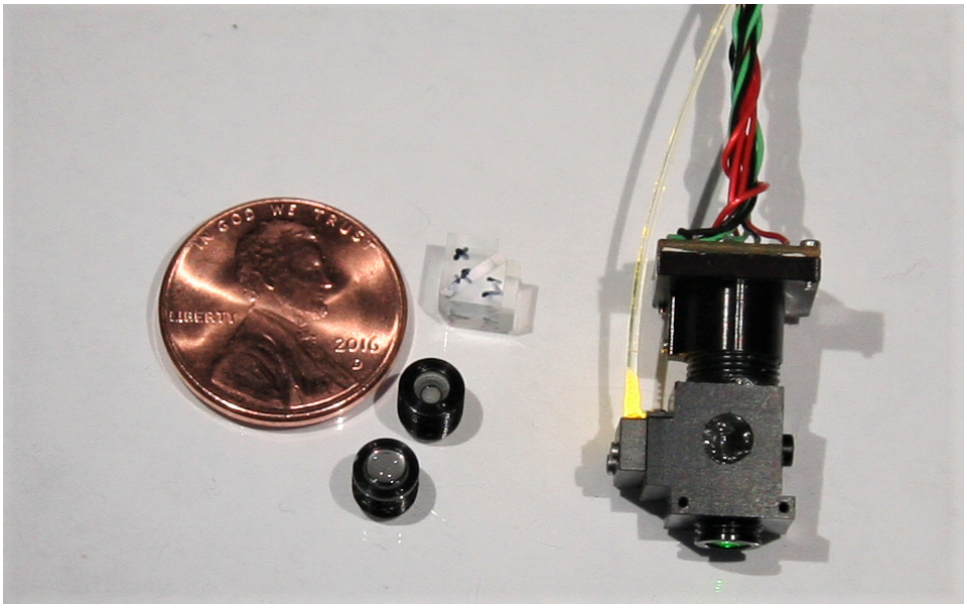

Figure 4.15: Gargantua microscope: assembled device, optics barrels, and filter cube.

4.2.1 Characterization Data

The salient characteristics of the Gargantua device are listed in the tables below. Any deviations from the design values are discussed in the subsequent section.

Physical Attributes

Table 4.2: Gargantua - Physical Attributes.

Weight	Size
2.96g	7 x 14 x 20mm

Optical Parameters

Table 4.3 describes the Optical Parameters of the Gargantua microscope. Table 4.4 shows the design and measured values for the magnification, FOV, and distortion of Gargantua. The magnification and FOV were measured using a grid target with 100μm spacing (Figure 4.16: B). Image was taken with the sensor in the middle of the focal track. Results compared favorably with prediction. The distortion was measured using the same images of the grid target, and calculated as 5.7%, similar to predicted value from Zemax. As distortion does not reduce resolution, this level was deemed acceptable.

Table 4.3: Gargantua - Optical Parameters.

Numerical Aperture	Working Distance	Magnification	Field of View
0.41	2,365μm	5.45x	0.911 x 0.703mm

Table 4.4: Comparison of FOV and distortion between theory and the integrated device measurements

	Design	Integrated Device (Focal Track - Middle)
Magnification	5.52	5.44
FOV	0.870 x 0.652mm	0.911 x .703mm
Distortion	5.0%	5.7%

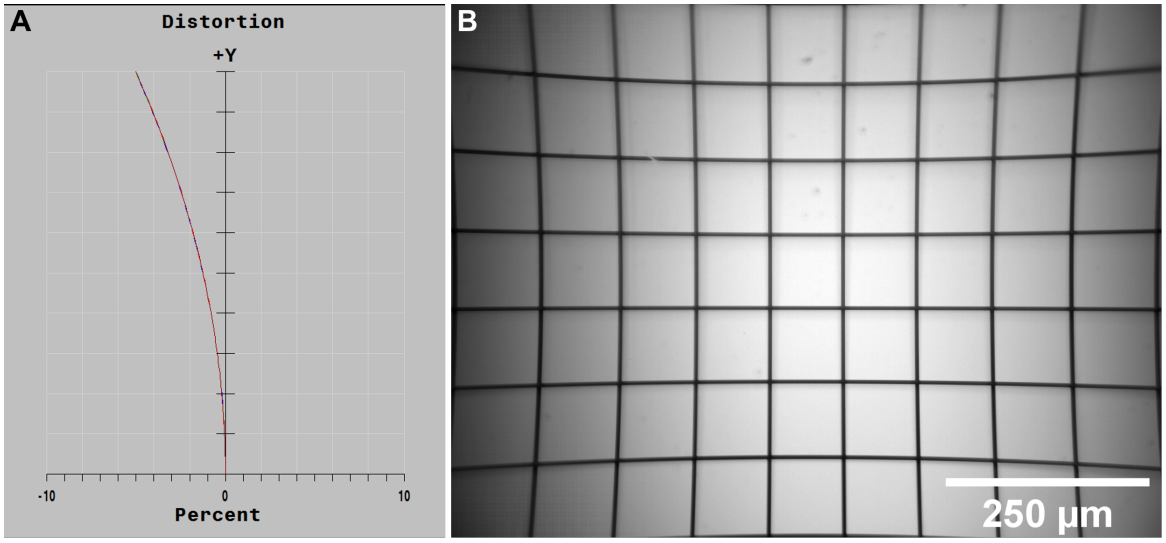

Figure 4.16: Field of view of Gargantua. A) Geometric distortion plot, calculated using Zemax. B) Image of a grid target with 100μm spacing. Image sensor was positioned in the middle of the focal track.

Digital Quantization

Table 4.5: Gargantua: Digital Quantization.

Frame Rate	Pixel Spacing	Sensor Bitrate
45.45fps	3.75μm 0.69μm at object plane	12-bit

Table 4.5 describes the Optical Parameters of the Salk Miniscope. It should be noted that with different initialization parameters the sensor is capable of 14-bit and 20-bit operation (with the addition of a third HiSpi data-lane). The lowest bit-rate was chosen to reduce bit-error over long distance transmission and improve signal integrity. The sensor was operated at 45.45fps at full resolution as well as 60 fps at 1280x720.

Imaging: Point Spread Function

Figure 4.17 shows images of the lateral and axial PSF of the Gargantua microscope. Table 4.6 shows the lateral and axial PSF FWHM values measured using the MetroloJ plugin, along with the R^2 values of the Gaussian fit.

Table 4.6: Gargantua - Imaging: Device PSF, measured in the center of the FOV. R^2 values taken from curve-fitting results.

	FWHM	R^2
x-axis	1.504μm	0.96410
y-axis	1.1352μm	0.98808
z-axis	17.185μm	0.97383

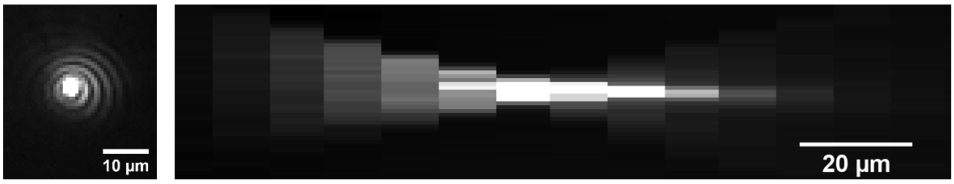

Figure 4.17: Gargantua: Lateral (Left) and axial (Right) PSF of the integrated device.

Imaging: Limit of Resolution

Table 4.7 and Figure 4.18 display the results of the LOR test at each location in the FOV. A small decrease in resolution is evident toward the edges of the FOV. At 220μm from the center, the resolution doubles the center value, and then decreases again.

Imaging: Modulation Transfer Function

Table 4.8 and Figure 4.19 display the results of the MTF test at each location in the FOV. There a moderate decrease in contrast toward the edges of the FOV, with the right-hand side

Table 4.7: Limit of resolution across the field of view

	Position in the Field of View				
	-420	-230	0	230	420
Tangential	0.59	0.71	0.59	0.83	1.25
Sagittal	1.00	0.83	0.71	0.59	0.53

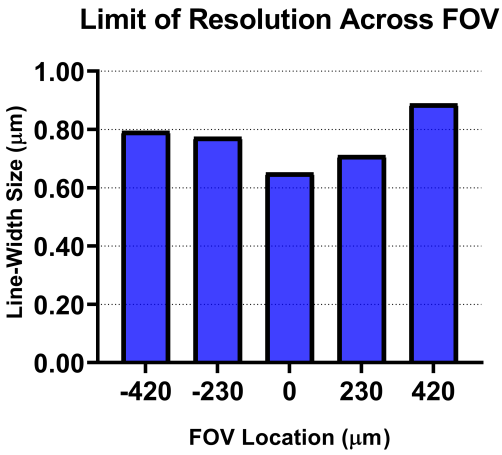

Figure 4.18: Gargantua microscope: The LOR measurements across the FOV in line-widths (μm).

regions noticeable worse the than the left side.

Table 4.8: MTF of the integrated device computed across the FOV. Values are in lp/mm for spatial frequency.

		Position in the Field of View				
		-420	-230	0	230	420
MTF10	Tangential	327	303	373	163	70
	Sagittal	444	303	303	257	397
MTF20	Tangential	233	233	280	140	47
	Sagittal	327	233	257	240	280
MTF50	Tangential	117	93	140	70	23
	Sagittal	140	117	140	93	117

Table 4.9: MTF across the FOV converted to line-width for intuitive comparison across devices. Values are in μm.

	Position in the Field of View				
	-420	-230	0	230	420
MTF10	1.3	1.7	1.5	2.4	2.1
MTF20	1.8	2.1	1.9	3.1	3.1
MTF50	3.9	4.8	3.6	6.1	7.1

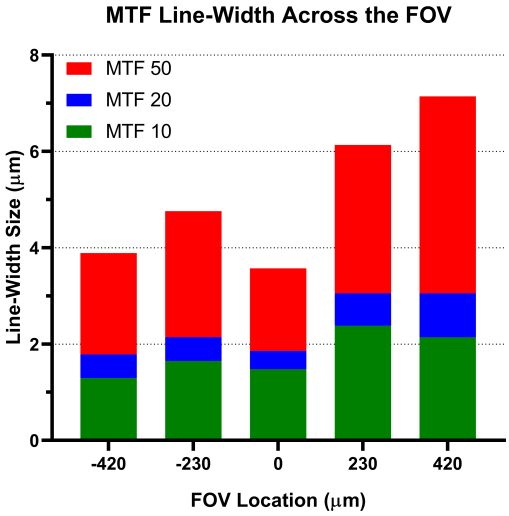

Figure 4.19: Gargantua: MTF10, 20 and 50 of the integrated device, across the FOV.

Color-Imaging Capability

Figure 4.20 shows an image of fluorescent beads, taken with Gargantua. All three colors of the beads are in focus, indicating good good correction. Beads are than the measures axial PSF values.

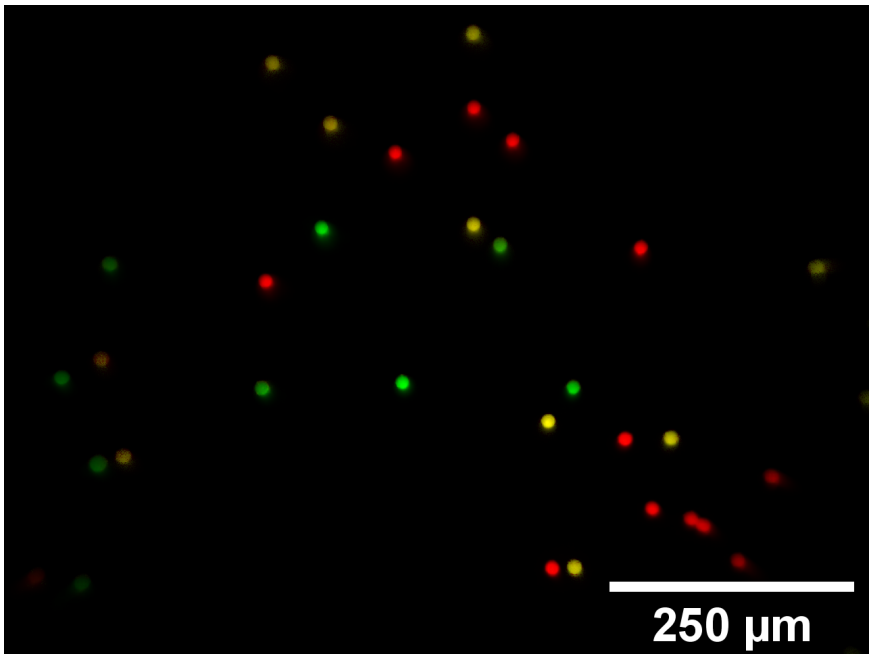

Figure 4.20: Color-imaging capability of Gargantua: B) 15μm polystyrene beads labeled with three fluorophores. All colors are in focus, indicating good correction for axial chromatic aberration

4.2.2 Design vs. Integrated Device

What follows are figures and tables comparing the performance of the theoretical design with the integrated device, tested using methods described in Chapter 2. The theoretical design was evaluated in Zemax Optical Modeling Software, using the following parameters:

Where appropriate, the Zemax figures were calculated using the polychromatic condition, across λ=500-620nm, consistent with the collection band of the installed fluorescence emission filter. The wavelength components were unweighted, as the device was designed for use with multiple fluorophores with overlapping spectral-bands.

Where relevant, the FOV of the Zemax figures was measured from the center (corresponding to zero on the horizontal axis), in coordinates of the rectangular image sensor: 2.4mm corresponded to the edges of the long side of the rectangular FOV, while 1.8mm corresponds to the edges of the short side of the FOV. The image sensor active area measured 4.8 x 3.6mm.

Point Spread Function

Table 4.10: Gargantua PSF : comparison of Zemax design, imaging optics with a filter simulant, and the integrated device. Values calculated using either K. Merten's MATLAB scripts (Zemax prediction and imaging optics measurements) or MetroloJ software (integrated device

PSF	Design	Imaging Optics	Integrated Device
x-axis	0.56μm	0.68μm	1.504μm
y-axis	0.56μm	0.68μm	1.352μm
z-axis	5.16μm	7.85μm	17.185μm

Table 4.10 and Figure 4.21 show the predicted and measured values of the PSF. PSF values of the imaging optics (along with a filter simulant) secured inside the test rig match closely with the Zemax predicted values, confirming the validity of the optical design as well as the lens fabrication process. However, the PSF values measured with the integrated device show a significant decrease in performance. The difference between the x-axis and y-axis FWHM values of the integrated device indicate astigmatism. I believe this is due to the filter cube, as it

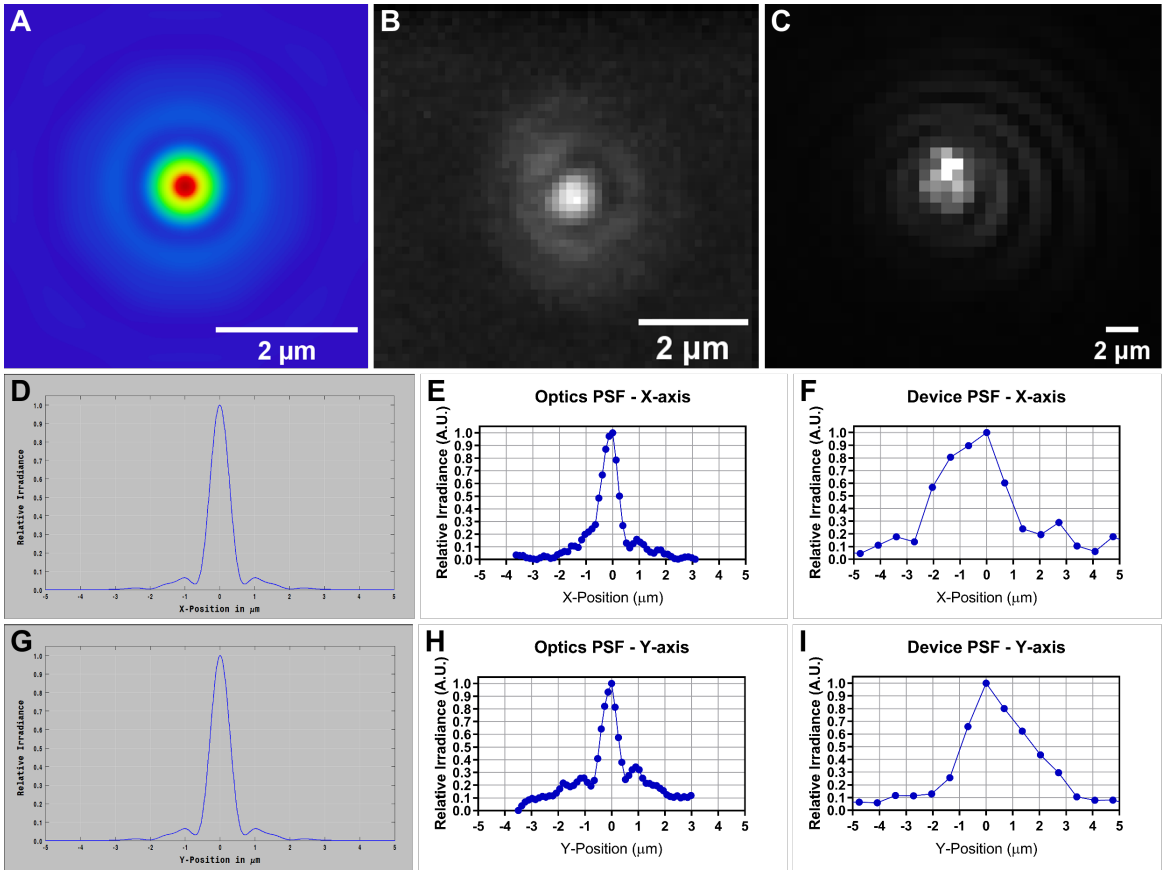

Figure 4.21: Gargatua: A, D, G) Theoretical PSF in 2D with cross-sections below. B, E, H) PSF of imaging optics, measured using the test rig. C, F, I) PSF of integrated device.

was missing from the test rig assembly. Improvements to the filter cube geometry and assembly process would most likely yield measurable gains in optical resolution. Nonetheless, the lateral PSF values of 1.4-1.5μm were strong, and should allow for imaging of most cell bodies, and many sub-cellular processes, in the context of sparse imaging.

Modulation Transfer Function

The MTF plots (Figure 4.22) are used to characterize the contrast of the microscope. The arrow indicates the Nyquist sampling limit of the image sensor, 736lp/mm based on the pixel spacing. The microscope displayed a good MTF50 line-width of 3.6μm in the center of the FOV, but with a small to moderate reduction in performance (~4-7μm MTF50 line-width)

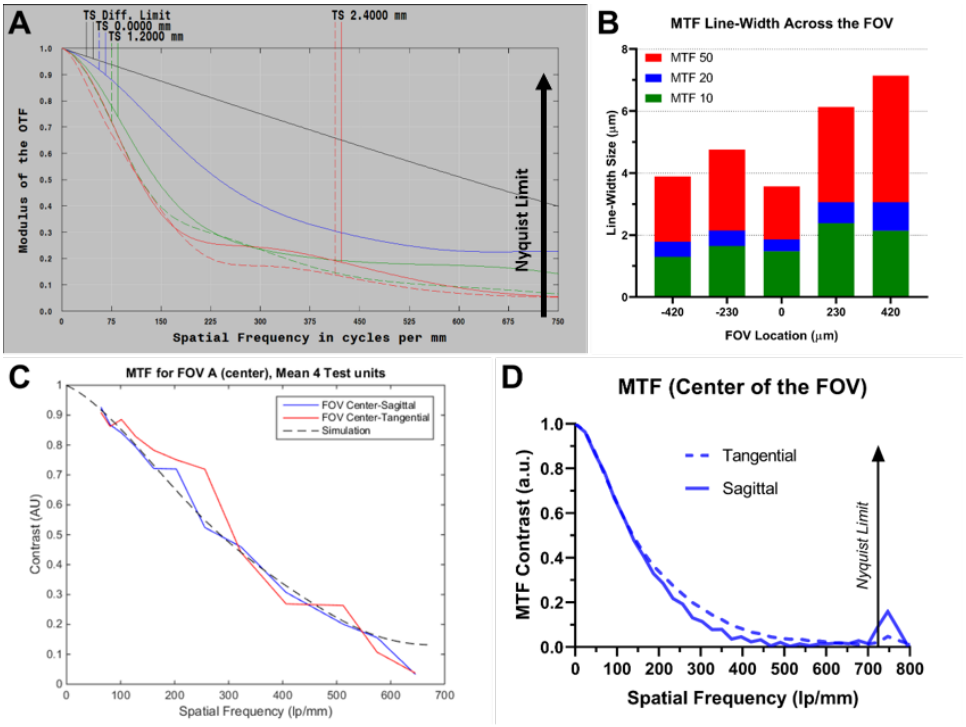

Figure 4.22: MTF of Gargantua across the FOV. A) Theoretical MTF, calculated in Zemax. B) MTF10, 20, and 50 across FOV. C) MTF of optics measured with a the test rig. Values are average of the 4 lens sets tested. D) Integrated device MTF in the center of the FOV.

toward the edges. The MTF values indicated that Gargantua would be able to resolve most cell bodies and many sub-cellular processes in moderately dense labeling environments, retaining a lot of that performance at edges of the FOV. Comparing the predicted and measured MTF curves (Figure 4.22A, D), the MT50 spatial frequency value in the center of the FOV was ~30% lower than predicted. However, comparing the predicted MTF with the measurements of the optics in the test rig, showed good agreement with the Zemax prediction. I suspected the difference in the integrated device values was due to the errors in filter cube fabrication, and that and improvements to the filter cube geometry and assembly process would most likely yield measurable gains in MTF contrast. Also of note was the decrease in MTF performance from the left to the right side of Figure 4.22B. This was most likely due to a tilt of the microscope during the testing procedure. Nonetheless, Gargantua showed strong results, with MTF 50 values at 4-7μm, and MTF10 at

1.5-2.5μm, across the field of view. This should allow Gargantua to image many cells, and a few sub-cellular processes, in densely labeled environments across the entire FOV.

4.3 Current and Future Applications

Gargantua has a significantly long working distance of 2.365mm, which is significant for biological experiments as the larger working distance allows for greater flexibility and fewer restrictions for the complex surgical preparation, and more importantly, allows for deeper and axial imaging of multiple cortical layers (e.g. imaging with intermediate optics) [8].

This miniature microscope also has a small PSF is significant for biological experiments as it allows us to reliably image sub-cellular processes in sparsely-labeled imaging environments. It is important to note that when tested separately, the optical system's measurements were closer to the design expectations Table 4.10. Additionally, with improvements to filter cube geometry and assembly procedures, the imaging quality of the integrated device is expected to improve significantly closer toward the optical system's performance Figure 4.22.

Our high-value LOR results shows spatial resolution across the entire FOV, not just at the center, demonstrating that the resolution does not degrade significantly out from the center and we are able to record consistent imaging quality across the entire FOV. This is significant for biological experiments as an increased FOV for imaging larger cellular networks will be negated if the optical system is not able to consistently resolve the cells across the FOV. Additionally, our characterization of the imaging quality using MTF indicates that we are able to successfully image with high resolution, even in densely-labeled environments (Figure 4.23). At the center of the FOV, our smallest line-width values for MTF20 and MTF10 (and their corresponding labeling densities) indicate that our miniature microscope can resolve cells of 1.79μm and 1.34μm, respectively (e.g. observing all neuronal and glial cell bodies, and even some sub-cellular processes). Furthermore, these smallest line-width values would improve as the labeling density becomes sparser.

Additionally, an upgraded sensor with smaller pixel spacing will lead to improved device performance as seen in Figure 4.22. The Nyquist limit states that the sensor pixel size should be at least one half of the PSF in order for the digital signal to maintain perfect fidelity; our sensor pixel is equal to our optical system's PSF. Calculations of our sensor Nyquist limit demonstrates that our optical system's ability to resolve images outperforms the sensor capabilities (the limiting resolution is set by the sensor, not the optical system), and future iterations of the device will include an updated sensor model.

As seen in Figure 4.23, the low PSF of Gargantua allows for the imaging of fine sub-cellular structures. The corrected axial chromatic aberration allows for imaging of multiple cell types.

Our microscope is currently the only one-photon miniature microscope that can image in three colors. Our integrated device was able to image the spectral range of 500-620nm, and when compared against Zemax calculations, our device is expected to have the capability of imaging into the near-infrared. Unfortunately, this cannot be confirmed due to the limitations of our filters, and we expect to confirm and demonstrate this capability in our future work. This ability to image multiple spectral bands is significant for biological experiments as it allows the concurrent observation of multiple genetically-distinct types or sub-types of cells. Figure 4.24 demonstrates the device's ability to image multiple colors prior to any software-based enhancements, despite utilizing a dual-band (limited wavelength discrimination) filter. This capability has significant implications for biology; Figure 4.24 panels E-F demonstrate unambiguous unmixing of three color channels despite significant overlap of the spectral bands. Future improvements in algorithms and sensors will make the unmixing of, and therefore, concurrent observations of more than three cell types possible using our microscope.

In addition to the performance improvements within the characterization categories, our microscope has significant advantages as the intentionally modular design increases functionality and the ease of implementing design improvements. For example, since our microscope was

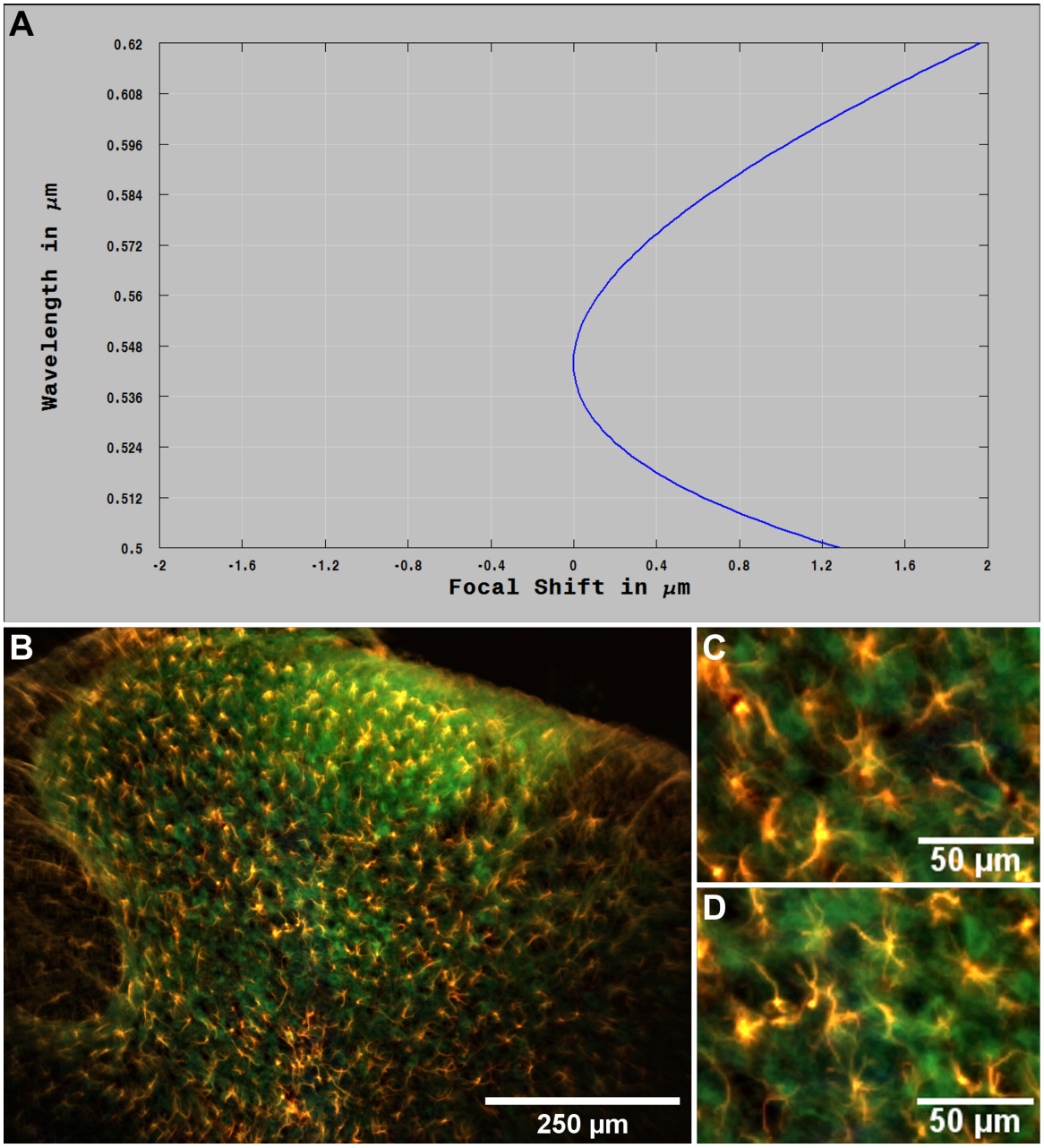

Figure 4.23: Gargantua: A) Theoretical chromatic focal shift. B) Image of spinal cord slice, with several distinct cell types stained with different fluorophores. C, D) Insets of 'B' processed through ImageJ plugin 'Subtract Background'.

designed to be easy to assemble and disassemble, parts like the filter cube are designed to able to be replaced with a different fluorescent filter set mid-experiment. Additionally, the modular design of the illumination modules allows for different types of experiments while using the same

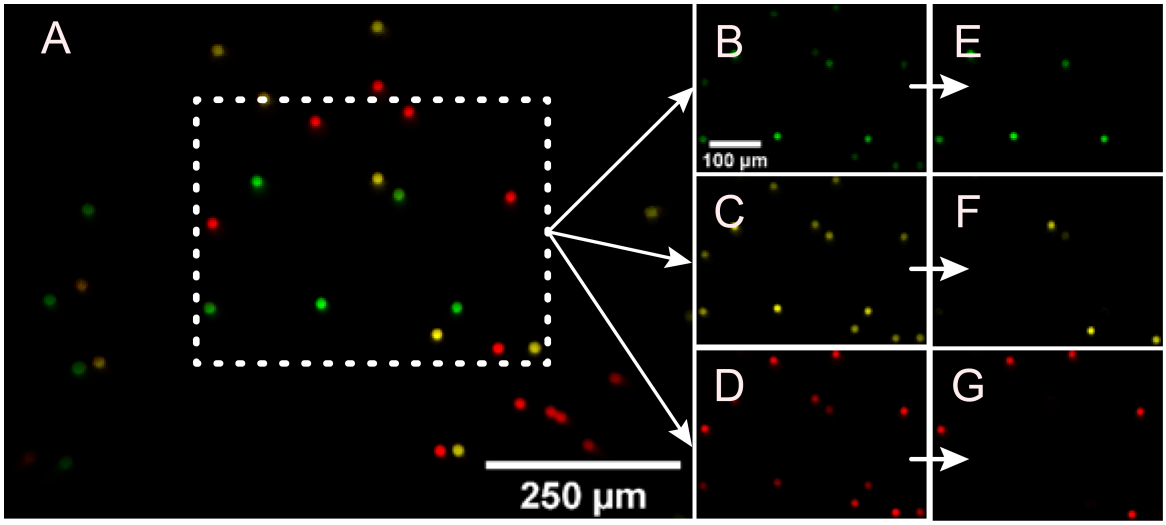

Figure 4.24: Left - 15μm polystyrene beads labeled with three fluorophores. Right - Individual color-channels before (left) and after (right) image processing using software pipeline described in Chapter 5. The processing eliminated color-channel cross-talk.

miniature microscope. This is significant for biological applications, as it allows the use of the microscope in optogenetic experiments. Optogenetic experiments, where light is used to interact with cells in living tissue that has been genetically modified, is highly desirable as it allows for the concurrent observation of multiple genetically-distinct types or sub-types of cells.

4.4 Summary

Acknowledgments

Chapter 4, in part, is currently being prepared for submission for publication of the material. Shekhtmeyster, Pavel; Nimmerjahn, Axel. The dissertation author was the primary investigator and author of this material.

Chapter 5

Software: Processing Pipeline

Due to the high number of cells labeled within the FOV, we wanted to utilize automatic methods for cell identification and signal extraction. Due to the particularities of images recorded with Gargantua, no software package which existed at the time could process the data out of the box. I developed an image-processing pipeline for data conditioning. Gargantua utilized the Poisson Non-Negative Matrix Factorization method (PNMF) [18], a color unmixing method which was robust to spectral overlap of the fluorescent emission. The ultimate goal was to utilize the robust open-source package Min1pipe [19] for the automated extraction of neuronal signals.

The following nine macros make up the pipeline which processes data files in batch with minimal user interaction: 'RawToTiff', 'Color Composite', 'DeleteBlackFrames', 'Background-Subtraction', 'PNMF' Macro and Plugin, 'ColorToMono, 'Min1pipe', 'BehavioralVideos', and 'BatchMoco'. Figure 5.1 is a flowchart that summarizes the workflow of the pipeline, and each is described further below.

What follows is a brief description of what each of the scripts and macros I wrote for the pipeline do. Other than Min1pipe and PNMF I wrote the scripts and macros. For Min1pipe my contribution was modifications to the code to run with our hardware, and made some modifications to the motion-estimation algorithm. For PNMF my contribution was modifications to memory

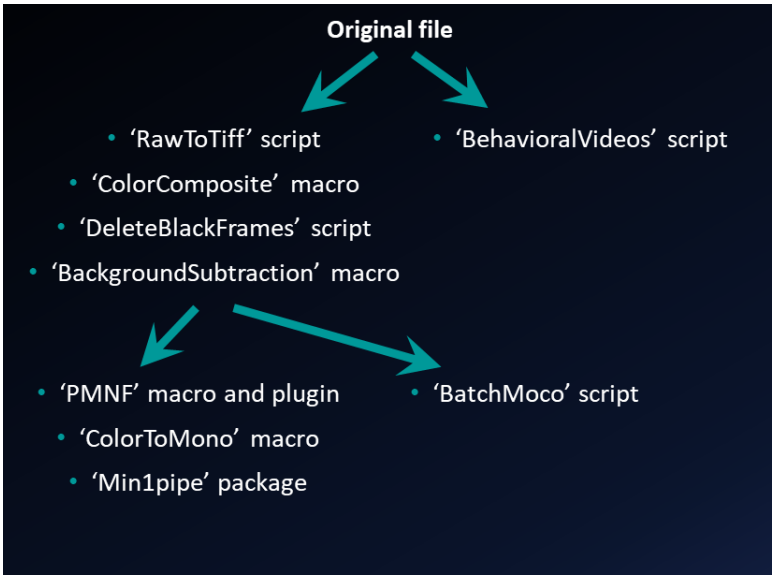

Figure 5.1: Flowchart of the software pipeline used for processing Gargantua data

management to allow usage with video data.

5.1 'RawToTiff' Script

The sensor outputs 12-bit image data saved in raw, binary little-endian format. This 'RawToTiff' MatLab script performs the following, in order:

1. Read-in raw data
2. Convert 12-bit to 16-bit. The 16-bit TIFF output was required in order to continue image processing using ImageJ.
3. Performs demosaicing using the Matlab 'demosaic' command (gradient-corrected linear interpolation algorithm). Data from a monochrome sensor skips this demosaicing step and is output as a single TIFF file.
4. Outputs three TIFF files corresponding to RGB color-channels.

5.2 ‘ColorComposite’ Macro

The ‘ColorComposite’ ImageJ macro performs the following, in order:

1. Read-in three TIFF files corresponding to RGB color-channels.
2. Performs denoising using the statistical threshold mean-filtering algorithm.
3. Outputs a single composite TIFF with three color-channels.

5.3 ‘DeleteBlackFrames’ Script

This ‘DeleteBlackFrames’ ImageJ macro allows synchronization of Gargantua recordings with data from behavioral camera. It performs the following, in order:

1. Read-in single composite TIFF with three color-channels. Can be used with one-channel monochrome data.
2. Locates black synchronization frames and removes them from the video.
3. Outputs composite TIFF in the same format as the input.

5.4 ‘BackgroundSubtraction’ Macro

Created automated technique that does what Matlab suggests you perform by hand. The ‘BackgroundSubtraction’ ImageJ performs the following, in order:

1. Read-in single composite TIFF with three color-channels. Can be used with one-channel monochrome data.

2. Performs blind-correction of illumination non-uniformity. Uses spatial frequency band-pass filter based on fast Fourier transform (FFT) method.

3. Performs background subtraction using blind Gaussian-filter based background, generated dynamically for each video frame. Can also be used with user-provided background image, though this method is not preferred.

4. Outputs composite TIFF in the same format as the input.

5.5 'PNMF' Macro and Plugin

Can be used with samples containing spatial and spectral overlap. The 'PNMF' ImageJ macro and ImageJ plugin performs the following, in order:

1. Read-in single composite TIFF with three color-channels.

2. Unmixes and isolates RGB channels into two or three independent color channels, corresponding to the emission spectral bands using the PNMF algorithm.

3. Outputs single composite TIFF file with multiple color channels corresponding to emission spectral bands.

5.6 'ColorToMono' Macro

The 'ColorToMono' ImageJ macro performs the following, in order:

1. Read-in composite TIFF output from PNMF macro.

2. Outputs individual files for each color channel, marking each file with the corresponding spectral band. For use with analysis packages that can only processes monochromatic data i.e. 'Min1pipe'.

5.7 ‘Min1pipe’ Package

The ‘min1pipe’ package for MatLab performs the following, in order:

1. Read-in monochrome TIFF of recording
2. Perform non-rigid motion-correction
3. Identify cell boundaries
4. Extracts neuronal signals from generated ROIs
5. Outputs both a motion-corrected video in .mat format and a .mat file identifying ROI boundaries and locations, along with the corresponding signal traces

*The ‘Min1pipe’ package performs analysis of neuronal signals only.

5.8 ‘BehavioralVideos’ Script

The behavioral camera image acquisition software saves each frame of the recorded data as individual TIFF files. The ‘BehavioralVideos’ script converts image-sequences into mulit-frame TIFF stacks for processing.

1. Asks user for input of directory of single-frame files.
2. Creates ordered-list of file names.
3. Reads-in image sequence one frame at time, in order.
4. Converts sequence into multi-frame TIFF stack.

5.9 'BatchMoco' Script

Used to improve speed and accuracy of 'Moco' rigid-motion-correction ImageJ plugin. Imaging awake animals introduces motion of tissue (from movements, breathing, etc.), so this script is used to remove motion within the frame by tracking the motion and translating each frame towards one set location. However, this plugin has trouble tracking low-contrast (high fluorescent background) images. My script creates a dummy-copy of the video, amplifies the features (e.g. blood vessels or cells) and makes them easier to track by 'Moco' by increasing the contrast. 'Moco' outputs a log of the frame motion, and my scrip uses the data to run a correction on the dummy-copy, saves the results, then applies the results to the original video.

1. Read-in video and make dummy-copy.
2. Run Gaussian filter to de-noise.
3. Amplifies the features by increasing contrast via 'Auto Thresholding' function.
4. Runs 'Moco' on the binary dummy-image, saves log.
5. Runs 'Moco' on original file using information from log.

Chapter 6

‘Odin’

Miniature Mesoscope Design

While performing experiments for the Salk Miniscope publication we noticed that the cellular response elicited by our stimuli would often times extend beyond the bounds of the field of view (FOV). This motivated the design of a new, large FOV mesoscope for freely-behaving mice.

There are a few tabletop mesoscopes and only one miniature mesoscope published. The tabletop mesocopes are complex and prohibitively expensive. The one miniature mesoscope is 33 grams and was designed to be worn by rats. At the time of writing, there were no published mesoscopes that could be used with freely-behaving mice.

In consideration of current published mesoscopes and our research goals, the following four goals were defined, in order of importance:

1. Large FOV: The first priority was to design a miniature microscope with a significantly greater FOV than the Salk Miniscope and Gargantua in order to better capture large-scale cellular activity.

2. Numerical Aperture (NA): The second goal was to design a device with an NA above 0.3.

3. Imaging Quality: The resolution goal was for the miniature microscope to resolve cells with greater than or equal to 6μm diameters.

4. Weight: In order to utilize this miniature microscope with mice, the goal was set to keep the weight under 10 grams.

5. Achromatic Wavelength Range (AWR): The microscope would be used to image GCaMP6f, a green fluorescence calcium reporter, so the AWR was set to 500-550nm.

What follows is the system design of Odin, categorized into the sections: Optomechanics and Housing, Optics, Illumination, and Electronics. Unfortunately, as of the time of this writing, the microscope fabrication is not yet complete, due to fabrication delays. As such, what is described below is based exclusively on the design of Odin Microscope.

6.1 System Design

6.1.1 Optomechanics and Housing

We defined two goals for the design of the optomechanics and housing of Odin. The first goal was to keep the weight of the device under 10g. The weight goal was determined during feasibility testing, where a mouse from the same genetic line as those used for the Salk Miniscope experiments was loaded to bear a spinal plate and a mock microscope. It was observed that the mouse could remain mobile with up to 10g of weight on the lumbar region of their spine.

The approach to keeping the housing light enough to allow non-restrained, freely moving mice behaviors was similar to that of Gargantua. PEEK was used for the majority of the housing components, due to its low density and strength. Since the sensor mount needed to be thermally conductive, it was fabricated from black anodized-aluminum.

The second goal, like Gargantua, was to keep the housing simple to fabricate and assemble. Since 3D printing still lacked the precision and material properties we required, it was concluded

to still not be a viable option. CNC milling was again selected as the fabrication technique for the housing components, which dictated the geometry of the components.

The housing was composed of seven components (the main body, optics barrels, filters, retainer, sensor mount, illumination module, and base plate), all of which were fabricated by Zera Development Company.

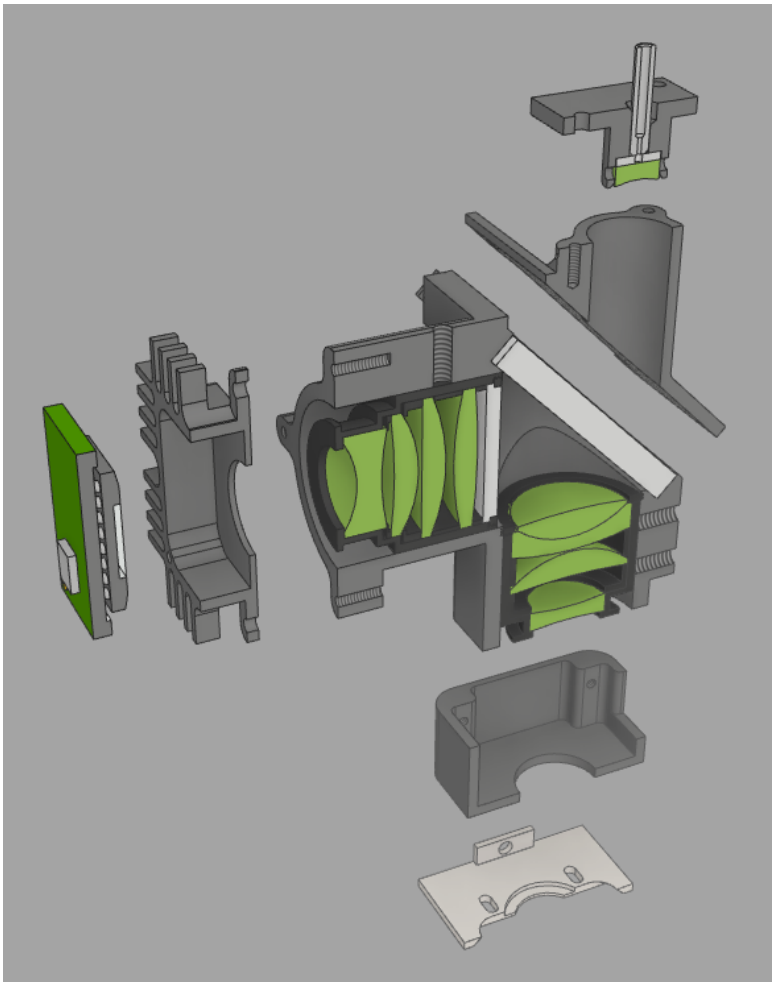

Figure 6.1: Odin: CAD model of housing, optics, optics barrels

Main Body

The main body was the central component of the housing and holds the optics barrels and dichroic mirror. The primary driver for the main body design was low weight while maintaining

optical alignment, a fact complicated by the fold geometry. I designed the main body to remove as much material as allowed when using CNC high-precision milling. Since the design of the fold geometry was predicted to complicate device assembly, the main body required high-tolerance fabrication. The critical dimensions were toleranced in Zemax to +/- 0.25 degree tolerance on dichroic mirror angle, and +/- 13μm tolerance on the lateral barrel alignment.

During tolerancing of the optical design, it became apparent that the air-space between the barrels along the optical axis was a sensitive parameter, and would need to be controlled during assembly. Therefore, the main body was designed to control this parameter by utilizing alignment plates. The alignment plates were mounted onto the main body during assembly, and were used as a guide to assist in securing the optical barrels 5.5mm away from the dichroic mirror. Once the barrels were secured using set screws (#0-80), the alignment plates were removed.

Optics Barrels

The imaging path of the microscope consisted of eight custom lens elements. The lenses required high-precision alignment in order to maintain the design performance. The imaging lenses are housed in two lens barrels, which are aligned inside the barrels during the fabrication process. Design of the internal optomechanics and constructions of the lens barrels was performed by the lens fabrication company, Optics Technology Inc.

Since the total weight of the device was a significant factor, the aluminum walls were designed at the minimum thickness of 0.6mm, and the retainer rings were designed to mount the lenses flush to the edge of the barrels. The optics barrels had a smooth outside diameter (no threads) to allow the design to utilize the thinnest walls. I also designed the outer geometry of the barrels with additional step-cuts to further reduce weight.

Filters

In order to lower the center-of-gravity of the device to facilitate mouse-mobility, I designed Odin to utilize a dichroic fold-mirror. The imaging path is folded at 90 degrees, allowing the relatively light illumination module to be mounted on top of the device while keeping the optics barrels closer to the animal's body. A short-pass dichroic mirror (495SP) from Semrock was used.

Since the mesoscope was designed to image one spectral band (GCaMP6f), the emission filter (ET-525/50m, Chroma) was integrated into the tube-lens barrel at the time of fabrication. This process was selected as it would greatly simplify assembly and assure light-tightness. The filter model was selected as it had the potential for future optogenetic experiments using excitation sources with λ>550nm.

The design did not include an excitation filter at it was intended for use with a fiber-coupled laser.

Dichroic Mirror Retainer

The dichroic mirror retainer, made from PEEK by Zera Development Company, was designed to secure the mirror into the main body on one side, and allowed for interface with the illumination module on the other. Though retainers are customarily not used for interfacing, this design required fewer connector pieces which contributed to the goal of a low-weight device.

Sensor Mount

The sensor mount was designed to use the same sensor as the Salk Miniscope and Gargantua (MTNM024, Aptina), but was configured in a different way since the housing geometry was significantly different. In anticipation of potential issues with bleed-through during concurrent-optogenetic experiments, I designed a space for an additional notch filter to ensure the microscope could be utilized for future experiments. Additionally, this sensor mount was designed to mate

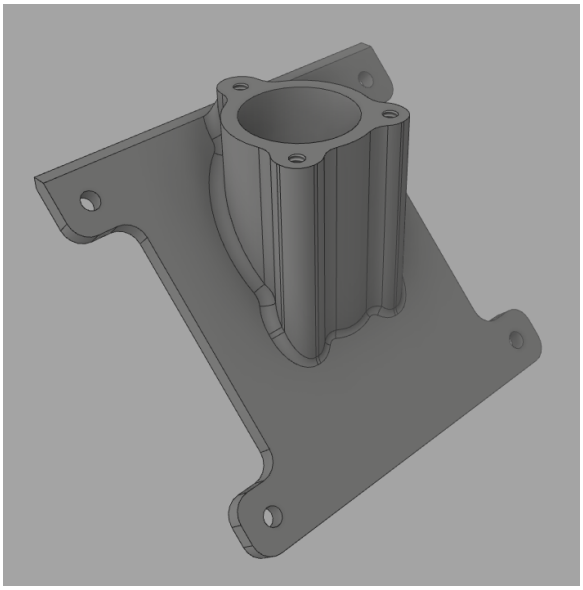

Figure 6.2: CAD of Odin's Dichroic Mirror Retainer.

directly with the main body without a thread-based focusing system. This capability was not included as it was rarely utilized during experiments with the Salk Miniscope and Gargantua, and the lack of this feature contributed to a lighter device. The sensor mount was designed with black anodized aluminum, which allowed the sensor mount to act as a heatsink for the image sensor.

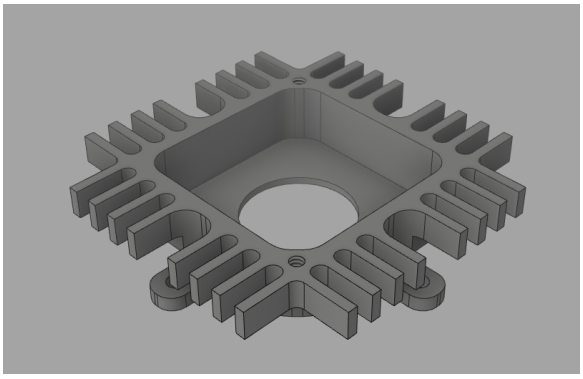

Figure 6.3: CAD of Odin's sensor mount.

Illumination Module

The illumination module was designed for use with laser light sources delivered through commercial silica-core MMF patch cords . It also included a collector lens (Demo3x, AGB1N0CS, Aptina Imaging Corp.), and custom spacer.

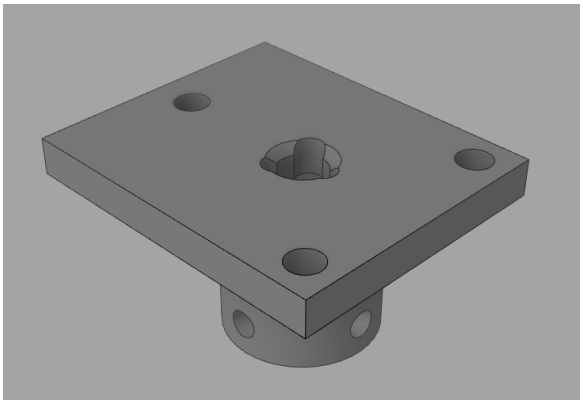

Figure 6.4: CAD of Odin's illumination module.

Base Plate

The baseplate was designed to facilitate chronic imaging experiments. The baseplate was designed to be mounted to the main body without a set mounting location, which allowed for focusing by translating the main body relative to the baseplate. The baseplate was secured using screws and the tensile force of the baseplate walls.

6.1.2 Optics

The goals for the optical system design of Odin were the large field of view (FOV), numerical aperture (NA), imaging quality, and achromatic wavelength range (AWR). I also focused on the magnification, optical track length, and working distance, and the goals were set as follows:

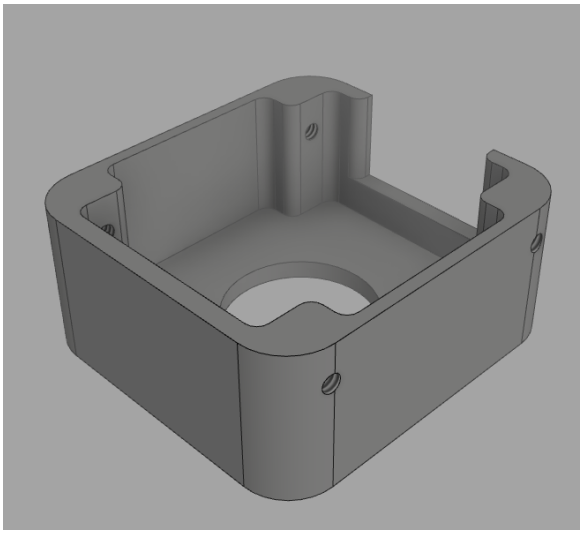

Figure 6.5: CAD of Odin's base plate.

Table 6.1: Design goals for Odin imaging optics.

Specification	Odin (Goals)
Field of View	3mm x 3mm
Numerical Aperture	> 0.3
Magnification	1.25
Optical Track Length	40
Working Distance	2000μm
RMS Spot Size Center	6μm
Acromatic Wavelength Range	500-550nm

Magnification was selected based on the size of the sensor and the resolution requirements. Specifically, a magnification of 1.25 would allow for a FOV of 3.84mm x 2.88mm, and a correspond pixel spacing of 3.0μm. Due to the fabrication limitations of spectral emission filters, the chief ray angle at the aperture stop was limited to +/- 15 degrees.

Imaging Path

A summary of the procedures for designing the imaging pathway was as follows:

The optical design was performed using Zemax optical modeling software and manual calculations. First, paraxial equations were used to create a general design form. Then, the

"Local Optimization" function in Zemax was used to create a realistic design using spherical lenses. Spherical lens elements were selected, and exotic glass materials were avoided, to simplify fabrication. The "Global Optimization" function was then used to generate 10-20 perspective design forms, and was run for five days. The most promising three-five designs were manually selected for further optimization and added to the Design Library. "Most promising" was defined based on the merit function value, perceived fabrication feasibility, and how distinct it was from other designs in the Library. The top designs from the library were then run through "Global Optimization" which produced new designs, then "Hammer Optimization" was run on the designs with the lowest merit function value. After repeating these steps and manually selecting and cultivating a design library from the hundreds of designs outputted, the two designs with the lowest merit function were then run through the "Hammer Optimization" function for one week each. The better design was then workshopped for the device.

The final imaging path consists of eight lens elements and I incorporated a field-stop into the design to improve resolution at the edges of the FOV. Figure 6.6 shows the optical layout Odin, while Figure 6.7 shows the optical prescription.

As this device was designed to be high-performing, it was predicted to be very sensitive to alignment, which informed the decision for designing alignment plates and a separate test rig to check the optical performance of the lens system prior to assembly into the final scope.

Fluorescence Filters

The goal was to image GCaMP6f. After exploring 23 filter options, the emission filter (ET525/50m, Chroma) and dichroic mirror (FF496-SDi01, Semrock) were selected based on maximizing fluorescence emission while minimizing spectral overlap.

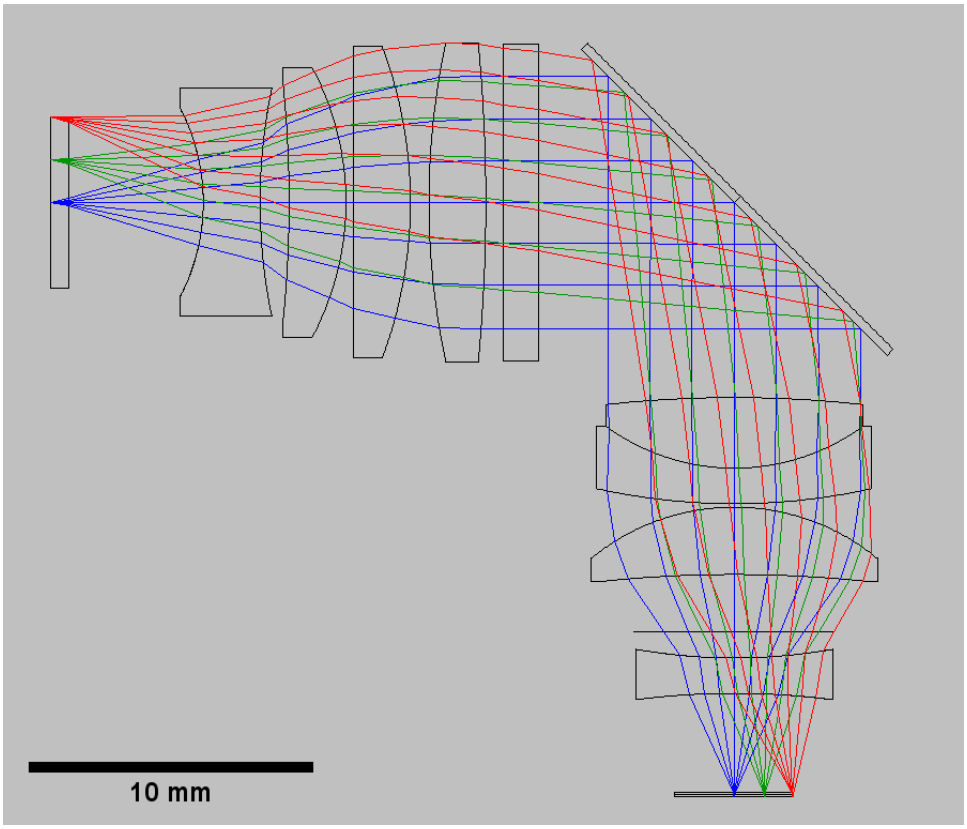

Figure 6.6: Imaging pathway of the Odin microscope

6.1.3 Illumination

The illumination design was considerably simplified from the design process for Gargantua. Since the goal for Gargantua included building multiple devices with multiple systems, it necessitated the demonstration of the feasibility of using low-cost LEDs.

Much was learned from the arduous, hand-fabricated process for Gargantua. Therefore, Odin was designed to be easily assembled with stock components. The necessity to use a more expensive illumination source (i.e. laser) was considered an acceptable compromise.

The illumination module was designed with commercial silica-core MMF patch cords , a collector lens , and a custom spacer, and was designed for use with a laser light source (λ = 473nm).

Surf	Type	Radius	Thickness	Glass	Diameter
OBJ	STANDARD	Infinity	0.4	N-BK7	6
1	STANDARD	Infinity	3.839877		5.951657
2	STANDARD	-5.743338	1.600023	N-SF66	5.368
3	STANDARD	15.70964	0.8187266		6.418
4	STANDARD	-32.7458	1.60104	S-LAH97	6.894
5	STANDARD	-8.05357	0.2169976		7.612
6	STANDARD	Infinity	1.600348	N-LAF34	8.46
7	STANDARD	-12.51519	0.5220518		8.774
8	STANDARD	21.5171	1.601503	S-LAH55V	9
9	STANDARD	-47.46657	0.5		9
10	STANDARD	Infinity	1	F_SILICA	8.92
11	STANDARD	Infinity	5.5		8.816
12	COORDBRK	-	0		-
13	STANDARD	Infinity	0	MIRROR	12.21416
14	COORDBRK	-	-5.5		-
STO	STANDARD	-33.34728	-1.989402	S-LAH97	7.124
16	STANDARD	6.137545	-1	N-SF66	7.238
17	STANDARD	17.95736	-0.1		7.754
18	STANDARD	-6.354997	-1.89487	S-LAH58	8.062
19	STANDARD	-35.8885	-1.609249		7.638
20	STANDARD	Infinity	-0.741		6.079522
21	STANDARD	15.94777	-0.9996236	N-SF66	5.534
22	STANDARD	-21.55705	-2.866169		5.098
23	STANDARD	Infinity	-0.037		4.05927
24	STANDARD	Infinity	0.1		4.054271
25	STANDARD	Infinity	-0.1	N-BK7	4.083375
IMA	STANDARD	Infinity			4.058435

Figure 6.7: Optical prescription of Odin.

6.1.4 Electronics

Odin uses the same sensor (Model-MT9M024, Aptina) and sensor board as the Salk Miniscope. The cabling twisting of wire pairs for the sensor cabling was outsourced to the Advanced Assembly Inc., and the same receiver board by was used for the design (USB-3 Board).

6.2 Integrated Device Characterization

Unfortunately, due to significant delays, the fabrication of the device is still in progress.

What follows is the characterization of the microscope design using Zemax Optical Modeling Software. Zemax is used to establish a baseline for performance expectations.

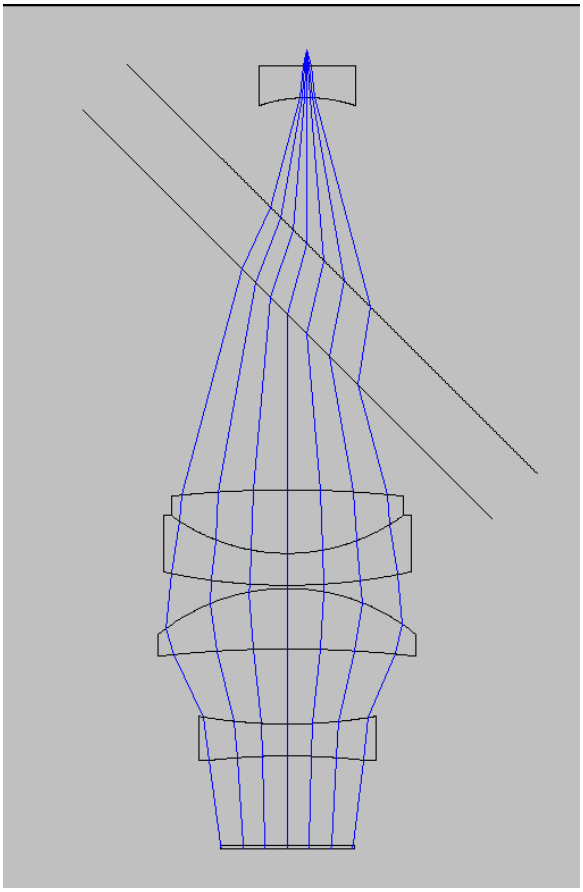

Figure 6.8: Odin illumination pathway from Zemax.

Odin was simulated using across 500-550nm wavelength range, corresponding to the collection bands of the fluorescence filter which was installed. Where relevant, the FOV is measured from the center (corresponding to zero on the horizontal axis), in coordinates of the rectangular image sensor: 2.4mm corresponds to the edges of the long side of the rectangular FOV, while 1.8mm corresponds to the edges of the short side of the FOV.

Where appropriate, the plots were calculates using the polychromatic condition, across λ=500-550nm, consistent with the collection band of the fluorescent emission filter. The wavelength components were unweighted.

The plot below shows the basic characteristics of the optical system. This system exhibits moderate geometric distortion, ~10% at the edge of the FOV. There is moderate vignetting present

due to the use of a field stop to correct off-axis aberrations.

The following plots are used to characterize the resolution of the microscope. The PSF cross section displays a well characterized peak. The FWHM of the PSF is a ~0.7μm., an excellent result which should allow for imaging of most cell bodies and subcellular processes.

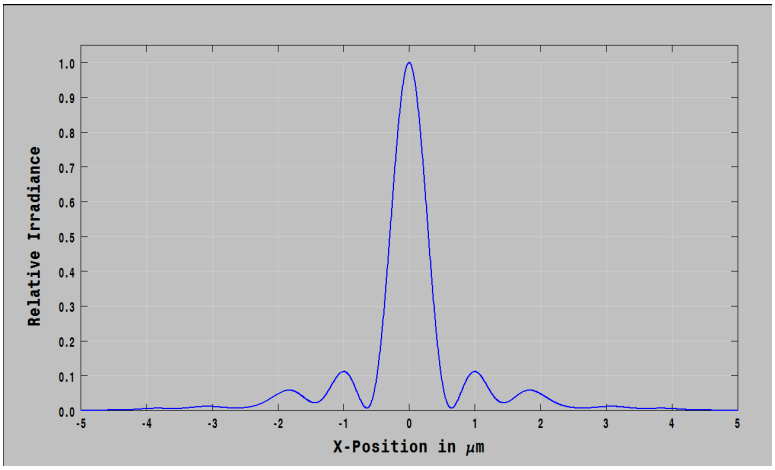

Figure 6.9: Theoretical PSF for Odin; calculated in Zemax.

The following plots are used to characterize the contrast of the microscope. The arrow indicated the Nyquist sampling limit of the image sensor, 184lp/mm based on the microscope magnification. The microscope displays a good MTF50 of 150lp/mm in the center of the FOV, and is moderately corrected for longitudinal chromatic aberration.

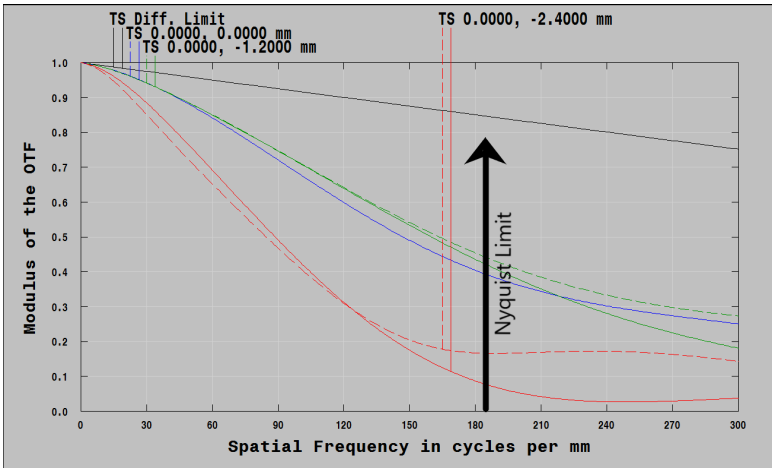

Figure 6.10: Theoretical MTF for Odin; calculated in Zemax.

6.3 Summary

As of the writing of this text, Odin is still in fabrication due to manufacturing delays.

Chapter 7

Conclusion

Figure 7.1 shows the improvements in image quality that were measured in Gargantua, compared to the image quality measured in the Salk Miniscope. Table 7.1 compares Gargantua performance with several other prominent miniature microscopes, published at the time of this writing. Gargantua improves upon those devices in most categories.

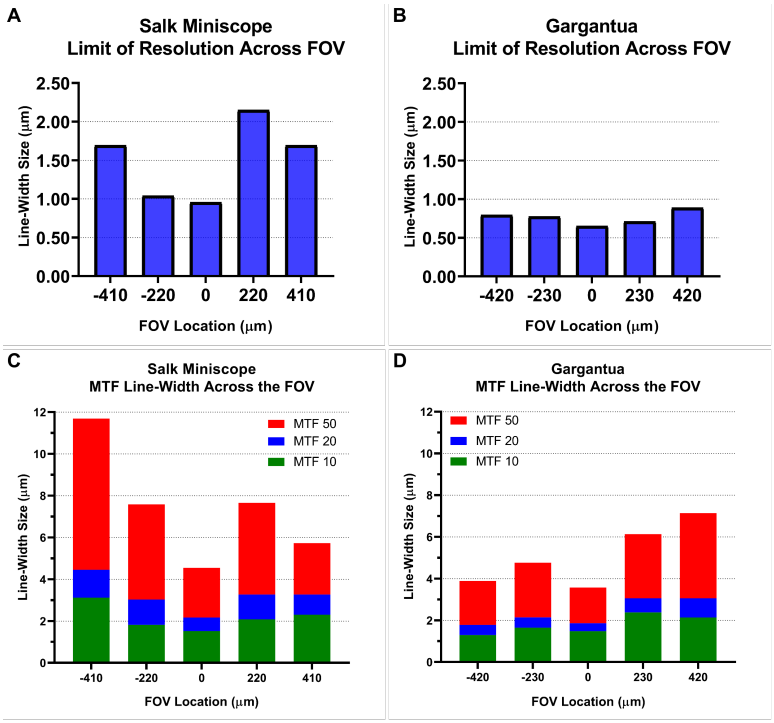

Figure 7.1: Comparison between the LOR and MTF of the Salk Miniscope (panels A, C) and Gargantua (panels B, D)

Table 7.1: Comparison of Gargantua's integrated device performance to other relevant works. Empty fields indicate data not reported in the respective publication.

		Integrated Device Characterization Data			
		Ghosh et al.	Glas et al.	Zong et al.	Gargantua
Physical Attributes	Size (mm)	8.4x13x22	-	10x10x10	7x17x20
	Weight (grams)	1.9	2.2	2.15	2.96
Optical Parameters	NA	0.45	0.5	0.8	0.41
	Working Distance (μm)	150-200	-	200	236.5
	FOV (μm)	650x490	1000x1000	130x130	911x703
Digital Quantization	Frame Rate (fps)	36	50	40	45
	Pixel Spacing (μm)	1.02-1.24	1.59	0.51	0.69
	Sensor Bit Depth (bits)	10	-	-	12
Imaging Quality	Lateral PSF: Center (μm)	-[1]	x = 3.52 y = 6.12	0.64	x = 1.50 y = 1.35
	Axial PSF: Center (μm)	-	33.35	3.35	17.19
	PSF: Average Edge (μm)	-	-	0.64	0.84
	MTF10/20/50: Center (μm)	-	-	-	1.48/1.86/3.57
	MTF10/20/50: Edge (μm)	-	-	-	1.72/2.42/5.52
	Color Imaging	No	No	Yes	Yes

[1] PSF data was reported for a single lens element, not the integrated system.

Bibliography

[1] Kohei J. Sekiguchi, Pavel Shekhtmeyster, Katharina Merten, Alexander Arena, Daniela Cook, Elizabeth Hoffman, Alexander Ngo, and Axel Nimmerjahn. Imaging large-scale cellular activity in spinal cord of freely behaving mice. Nature Communications, 7:11450, 2016.

[2] Kunal K Ghosh, Laurie D Burns, Eric D Cocker, Axel Nimmerjahn, Yaniv Ziv, Abbas El Gamal, and Mark J Schnitzer. Miniaturized integration of a fluorescence microscope. Nature Methods, 8(10):871–878, oct 2011.

[3] Annet Glas, Mark Hübener, Tobias Bonhoeffer, and Pieter M. Goltstein. Benchmarking miniaturized microscopy against two-photon calcium imaging using single-cell orientation tuning in mouse visual cortex. PLOS ONE, 14(4):e0214954, apr 2019.

[4] Denise J. Cai, Daniel Aharoni, Tristan Shuman, Justin Shobe, Jeremy Biane, Weilin Song, Brandon Wei, Michael Veshkini, Mimi La-Vu, Jerry Lou, Sergio E. Flores, Isaac Kim, Yoshitake Sano, Miou Zhou, Karsten Baumgaertel, Ayal Lavi, Masakazu Kamata, Mark Tuszynski, Mark Mayford, Peyman Golshani, and Alcino J. Silva. A shared neural ensemble links distinct contextual memories encoded close in time. Nature, 534(7605):115–118, jun 2016.

[5] Oliver Skocek, Tobias Nöbauer, Lukas Weilguny, Francisca Martínez Traub, Chuying Naomi Xia, Maxim I. Molodtsov, Abhinav Grama, Masahito Yamagata, Daniel Aharoni, David D. Cox, Peyman Golshani, and Alipasha Vaziri. High-speed volumetric imaging of neuronal activity in freely moving rodents. Nature Methods, 15(6):429–432, jun 2018.

[6] Weijian Zong, Runlong Wu, Mingli Li, Yanhui Hu, Yijun Li, Jinghang Li, Hao Rong, Haitao Wu, Yangyang Xu, Yang Lu, Hongbo Jia, Ming Fan, Zhuan Zhou, Yunfeng Zhang, Aimin Wang, Liangyi Chen, and Heping Cheng. Fast high-resolution miniature two-photon microscopy for brain imaging in freely behaving mice. Nature Methods, 14(7):713–719, jun 2017.

[7] Benjamin B. Scott, Stephan Y. Thiberge, Caiying Guo, D. Gowanlock R. Tervo, Carlos D. Brody, Alla Y. Karpova, and David W. Tank. Imaging Cortical Dynamics in GCaMP Transgenic Rats with a Head-Mounted Widefield Macroscope. Neuron, 100(5):1045–1058.e5, dec 2018.

[8] Mark L. Andermann, Nathan B. Gilfoy, Glenn J. Goldey, Robert N S Sachdev, Markus Wölfel, David A. McCormick, R. Clay Reid, and Michael J. Levene. Chronic Cellular Imaging of Entire Cortical Columns in Awake Mice Using Microprisms. Neuron, 80(4):900–913, 2013.

[9] Fabrice P. Cordelières. MetroloJ [ImageJ Documentation Wiki].

[10] Tiago Ferreira. Find Peaks - ImageJ, 2014.

[11] Sharon A. Haymes, Kenneth F. Roberts, Alan F. Cruess, Marcelo T. Nicolela, Raymond P. LeBlanc, Michael S. Ramsey, Balwantray C. Chauhan, and Paul H. Artes. The letter contrast sensitivity test: Clinical evaluation of a new design. Investigative Ophthalmology and Visual Science, 47(6):2739–2745, 2006.

[12] Aries Arditi. Improving the design of the letter contrast sensitivity test. Investigative Ophthalmology and Visual Science, 46(6):2225–2229, 2005.

[13] Bradley E Dougherty, Roanne E Flom, and Mark a Bullimore. An Evaluation of the Mars Letter Contrast. Optometry & Vision Science, 82(11):970–975, 2005.

[14] Peter G. J. Barten. Physical model for the contrast sensitivity of the human eye. Human Vision, Visual Processing, and Digital Display III, 1666(August 1992):57, 1992.

[15] Peter G. J. Barten. Formula for the contrast sensitivity of the human eye. Image Quality and System Performance XII, 5294(December 2003):231–238, 2003.

[16] Warren J. Smith. Modern lens design. McGraw-Hill, 2nd edition, 2005.

[17] Carles Mitja, Jaume Escofet, Aura Tacho, and Raquel Revuelta. Slanted Edge MTF - Image J, 2011.

[18] Richard A. Neher, Mišo Mitkovski, Frank Kirchhoff, Erwin Neher, Fabian J. Theis, Richard A. Neher, Mišo Mitkovski, Frank Kirchhoff, Erwin Neher, and André Zeug. Blind source separation techniques for the decomposition of multiply labeled fluorescence images. Biophysical Journal, 96(9):3791–3800, 2009.

[19] Jinghao Lu, Chunyuan Li, Jonnathan Singh-Alvarado, Zhe Charles Zhou, Flavio Fröhlich, Richard Mooney, and Fan Wang. MIN1PIPE: A Miniscope 1-Photon-Based Calcium Imaging Signal Extraction Pipeline. Cell Reports, 23(12):3673–3684, jun 2018.